Vol. 25, No. 2(2026) Fen26778
Revista Mexicana de Ingeniería Química

Direct numerical simulation of the two-dimensional differentially heated square cavity at high Rayleigh numbers ($Ra \leq 10^{12}$)

Simulación numérica directa de la cavidad cuadrada calentada diferencialmente en dos dimensiones a números de Rayleigh altos ($Ra \leq 10^{12}$)

F.I. Molina-Herrera[1], H. Montes-Rosales[3], N.E. Maldonado-Sierra[4], M.A. Sandoval-Hernández[5], G.M. Martinez-González[3], M.L. López-González[1], H. Jiménez-Islas[2]*

[1]*Departamento de Ingeniería Agroindustrial. Universidad de Guanajuato. Av. Ing. Javier Barros Sierra 201, esq. Av. Baja California, Ejido Santa María del Refugio, Celaya, Gto, 38110, México.*

[2]*Departamento de Ingeniería Bioquímica y Ambiental. Tecnológico Nacional de México en Celaya. Antonio García Cubas Pte. #600 esq. Av. Tecnológico, Celaya, Guanajuato, 38010, México.*

[3]*Departamento de Ingeniería Química. Tecnológico Nacional de México en Celaya. Antonio García Cubas Pte. #600 esq. Av. Tecnológico, Celaya, Guanajuato, 38010, México.*

[4]*Departamento de Ingeniería en Alimentos. Universidad Politécnica de Guanajuato. Av. Universidad Sur #1001, Cortázar, Guanajuato, 38496, México.*

[5]*Universidad Politécnica Metropolitana de Hidalgo, Tolcayuca 43860, Hgo, México.*

Received: January 30, 2026; Accepted: April 15, 2026

Abstract

This work presents a numerical study of natural convection in a 2-D differentially heated square cavity at high Rayleigh numbers ($Ra \leq 10^{12}$), using a dimensionless formulation of the incompressible Navier-Stokes equations. The problem was solved using the finite element method on an orthogonal quadrilateral mesh with boundary-layer-type refinement along the hot and cold vertical walls to resolve the steep thermal and hydrodynamic gradients near the boundaries. A systematic grid-independence study identified a mesh with 100 boundary-layer elements as sufficient to capture the relevant near-wall structure. Numerical consistency was assessed through macroscopic heat-balance verification, mesh-quality evaluation, and transient monitoring of the wall-integrated Nusselt number. Accuracy was further examined by comparison with classical and modern reference data available in the literature. The results show very good agreement with benchmark solutions across a wide range of Rayleigh numbers, and a consistent rise in heat transfer as Ra increases. In addition, a power-law regression of the computed data over $10^3 \leq Ra \leq 10^{11}$ predicts the $Ra = 10^{12}$ result with excellent agreement. The steady-state and transient simulations converge to nearly identical Nusselt values at high Rayleigh numbers, confirming the robustness of the proposed numerical strategy. Overall, the adopted meshing approach provides stable and numerically consistent reference solutions for the classical 2-D differentially heated cavity benchmark at high Rayleigh numbers.

Keywords: Differentially heated square cavity; Natural convection; Rayleigh number; Finite element method; Boundary-layer mesh.

Resumen

Este trabajo presenta un estudio numérico de la convección natural en una cavidad cuadrada, diferencialmente calentada, en 2D, a números de Rayleigh elevados ($Ra \leq 10^{12}$), utilizando una formulación adimensional de las ecuaciones de Navier-Stokes para flujo incompresible, sin recurrir a modelos de turbulencia. El problema se resolvió mediante el método de elementos finitos sobre una malla cuadrangular ortogonal, con refinamiento tipo capa de frontera a lo largo de las paredes verticales, caliente y fría, respectivamente, para capturar los gradientes térmicos e hidrodinámicos intensos que se desarrollan cerca de las fronteras. Un estudio sistemático de independencia de malla permitió identificar una malla con 100 elementos de capa de frontera como suficiente para capturar la estructura relevante en la región cercana a la pared. La consistencia numérica se evaluó mediante la verificación del balance macroscópico de calor, la evaluación de la calidad de la malla y el monitoreo dinámico del número de Nusselt en las paredes verticales. Además, la precisión se evaluó mediante la comparación con datos de referencia clásicos y modernos publicados en la literatura. Los resultados muestran una muy buena concordancia con soluciones de referencia en un amplio intervalo de valores de Ra y un incremento consistente en la transferencia de calor a medida que aumenta Ra. Adicionalmente, una regresión del tipo potencia de los datos calculados en el intervalo $10^3 \leq Ra \leq 10^{11}$ predice el resultado para $Ra = 10^{12}$ con excelente concordancia. Las simulaciones en estado estacionario y dinámico convergen hacia valores de Nusselt prácticamente idénticos para números de Rayleigh elevados, lo que confirma la robustez de la estrategia numérica propuesta. En síntesis, el enfoque de mallado adoptado produce soluciones de referencia estables y numéricamente consistentes para el problema clásico de cavidad calentada diferencialmente en 2D, con números de Rayleigh elevados.

Palabras clave: Cavidad cuadrada diferencialmente calentada; Convección natural; Número de Rayleigh; Método de elemento finito; Malla de capa de frontera.

*Corresponding author. E-mail: hugo.jimenez@itcelaya.edu.mx ;
https://doi.org/10.24275/rmiq/Fen26778 *ISSN*:1665-2738, *issn-e*: 2395-8472

1 Introduction

The study of natural convection in differentially heated square cavities is a classical problem in fluid mechanics and heat transfer. It has been widely used as a benchmark for validating numerical methods, discretization algorithms, and turbulence models. Its relevance lies in the fact that, despite the system's geometric simplicity, it captures complex physical phenomena, including the formation of thermal and hydrodynamic boundary layers, the development of vortical structures, and the transition from laminar to turbulent flow as the Rayleigh number (Ra) increases. These characteristics have established differentially heated cavities as an indispensable model for investigating transport processes and for practical applications, including electronic component cooling, thermal insulation in reactors, energy storage systems, passive ventilation in buildings, and the optimization of heat transfer devices.

Following the pioneering work of De Vahl Davis (1983), this problem has become a standard benchmark case, providing reliable Nusselt number values and temperature profiles for $10^3 \leq Ra \leq 10^6$. One year later, Markatos and Pericleous (1984) introduced the k–ε turbulence model for enclosed cavities, extending the analysis up to Ra = 10^{16}. Their results agreed with those of De Vahl Davis (1983) for Ra ≤ 10ˆ6; however, at high Rayleigh numbers, the model overestimated the Nusselt number, indicating limitations in its representation of turbulent structures. Shortly thereafter, Henkes and Hoogendoorn (1989) investigated the transition to unstable flow regimes for Rayleigh numbers between 2×10^6 and 10^8, identifying the onset of oscillatory behavior and chaotic regimes. These authors emphasized that heat transfer does not increase monotonically due to temporal fluctuations, as evidenced by periodic variations in the Nusselt number. During the same decade, Xin and Le Quéré (1994) extended the analysis using two-dimensional direct numerical simulations up to Ra = 10^{10}. Their results demonstrated the transition to chaotic behavior, characterized by turbulent structures and time-dependent fluctuations of the Nusselt number, confirming the strong dependence of heat transfer on the flow regime.

Subsequently, Dixit and Babu (2006) conducted a numerical evaluation of natural convection up to Ra = 10^{10}, highlighting the importance of mesh refinement for accurately predicting boundary-layer dynamics. They also observed that insufficient spatial discretization leads to an overestimation of the Nusselt number, highlighting the problem's strong sensitivity to mesh resolution and spatial accuracy. Trias *et al.* (2007) made advances by conducting direct numerical simulations in both two- and three-dimensional configurations for Ra = 6.4×10^8, Ra = 2×10^9, and Ra = 1×10^{10}. These authors demonstrated that, in three-dimensional simulations, large-scale vortical structures break down more rapidly, leading to stronger thermal stratification and higher Nusselt numbers than in two-dimensional simulations. These findings confirmed the importance of three-dimensional effects in heat transfer. Subsequently, Goloviznin *et al.* (2016) extended two-dimensional direct numerical simulations using spectral techniques up to Ra = 10^{14}, capturing in detail the fully developed turbulent regime and the formation of extremely thin boundary layers. Their results showed good agreement with trends previously reported in direct numerical simulation studies, thereby consolidating their use as reference data for high-Rayleigh-number conditions.

Along the same lines, Hernández-López *et al.* (2016) employed the heatlines concept to analyze natural convection in closed and ventilated cavities, covering Rayleigh numbers ranging from 10^3 to 10^{12}. Their studies showed that as the Rayleigh number increases, heat transfer becomes predominantly advective and the thermal boundary layers are confined near the walls, reinforcing the relevance of the cavity problem as a benchmark test case for evaluating both direct numerical simulations and turbulence models in extreme natural-convection regimes. In parallel, several authors have employed turbulence models based on the Reynolds-Averaged Navier-Stokes (RANS) framework, which decomposes flow variables into mean and fluctuating components and solves only the time-averaged governing equations (Wilcox, 1993). This approach enables the representation of the global effects of turbulence through additional transport terms and closure models, thereby significantly reducing the computational cost compared with direct numerical simulation or large eddy simulation.

In this context, the most widely used models are the k–ε model, which represents turbulent kinetic energy (k) and its dissipation rate (ε), and the k–ω model, which employs the specific dissipation rate (ω) instead of ε and exhibits improved performance in near-wall regions. Igci and Arici (2016) evaluated these models in square cavities under natural convection at high Rayleigh numbers and found that they accurately reproduce the global trends in heat transfer and flow development. Nevertheless, they also reported that Reynolds-Averaged Navier-Stokes models tend to overestimate turbulent energy dissipation, which leads to discrepancies in the prediction of convective intensity and the Nusselt number when compared with results obtained through direct numerical simulation (Jones and Launder, 1972; Trias *et al.*, 2007; Trias *et al.* 2010; Choi and Kim, 2012; Cintolesi *et al.*, 2015; Zamora-Cisneros and Ruiz Martínez, 2023). It is also important to emphasize that, unlike Reynolds-Averaged Navier–Stokes approaches, Large Eddy Simulation explicitly resolves the large-scale eddies and models only the smaller scales, providing a higher level of physical detail at an intermediate computational cost. In contrast, Direct Numerical Simulation resolves all flow scales without closure models, offering the highest level of accuracy, though at an extremely high computational cost. It should be noted that, as computational platforms continue to advance, this limitation is expected to become less restrictive in the medium term (Trias *et al*., 2010).

Recent studies have reinforced the importance of having accurate reference data for describing natural convection in cavities. Weppe *et al.* (2022) demonstrated, using both experimental and numerical approaches, that three-dimensional cavities with internal obstacles exhibit complex instabilities, such as Tollmien–Schlichting waves and oscillatory buoyant jets, which Reynolds-Averaged Navier-Stokes models fail to reproduce with sufficient accuracy. These findings highlight the need for more detailed approaches, such as Large Eddy Simulation or Direct Numerical Simulation (Abbassi *et al.*, 2018; Duchaine, 2010). In a complementary manner, Choi and Kim (2012) reviewed the performance of various Reynolds-Averaged Navier-Stokes turbulence models, emphasizing that, although they provide a computationally efficient alternative, they exhibit systematic deficiencies in boundary layer prediction and in the representation of heat transfer under strongly stratified regimes, leading to discrepancies with respect to both experimental data and numerical simulation results.

Along the same line, El Hattab and Lafdaili (2022) employed a two-dimensional *k*–*ε* model to analyze cavities filled with nanofluids under the influence of magnetic fields, showing that this type of approximation allows the exploration of global trends but does not accurately capture the transition to the turbulent regime or the instabilities characteristic of high Rayleigh numbers. These studies indicate that, although three-dimensional simulations provide a more representative description of flow complexity, their high computational cost still limits access to extreme regimes (Wang *et al.*, 2022; Villa-Ortiz and Koloszar, 2023; Ghoben and Hussein, 2022; Weppe *et al.*, 2022). In this context, two-dimensional numerical simulations constitute an appropriate strategy for generating benchmark reference data within the adopted formulation. Such results enable a detailed numerical characterization of the thermal and flow fields in the square cavity model, thereby providing a useful basis for validating numerical algorithms and comparing them with more complex formulations. At high Rayleigh numbers, the physics of the problem is governed by extremely thin thermal and hydrodynamic boundary layers and by intense gradients near the hot and cold walls, respectively. In this regime, the accuracy of Nusselt number predictions depends critically on ultrafine mesh refinement in the wall-normal direction; otherwise, inadequate mesh resolution introduces significant errors in the Nusselt number calculation.

Reynolds-Averaged Navier-Stokes models, such as the *k*–*ε* and *k*–*ω* formulations, capture global trends at reduced computational cost but exhibit systematic biases in the near-wall regions at high Rayleigh numbers. These biases lead to an underestimation of natural convection, excessive smoothing of gradients, and, consequently, an underprediction of Nusselt numbers (Trias *et al.*, 2007; Igci and Arici, 2016). Simulations based on Large Eddy Simulation models improve the level of detail at large scales, although they still incur high computational cost (Cintolesi *et al.*, 2015; Weppe *et al.*, 2022). In contrast, Direct Numerical Simulation, by resolving all flow scales without closure models, remains the reference approach for accurately quantifying heat transfer, near-wall structure, and regime transitions. Goloviznin *et al.* (2016) also showed that, for the De Vahl Davis cavity (1983), in both two-dimensional and three-dimensional configurations and without the use of turbulence models, the average Nusselt number follows reference trends over a wide range of Rayleigh numbers and exhibits good agreement with classical results at low to intermediate Rayleigh numbers in the convective regime.

In addition, the Nusselt number exhibits a representative power-law behavior of the form $\mathrm{Nu} \approx 0.182 \times \mathrm{Ra}^{0.275}$ (for $\mathrm{Pr} \approx 0.71$) (Cortés-Avendaño *et al.*, 2023; Welti-Chanes *et al.*, 2005). This behavior reinforces the assertion that the Nusselt number is a reliable metric for validating the accuracy of cavity simulations and confirms the suitability of direct numerical simulation as a standard method for evaluating turbulence models and numerical strategies at high Rayleigh numbers. Additional evidence indicates that the numerical methodology and mesh resolution directly condition the accuracy of the predictions. As the mesh becomes progressively finer, the Nusselt number values are expected to approach converged values, as established by differential calculus. However, oscillatory behavior around a central value may arise from factors such as the discretization scheme, solution methods, and the computational platform.

On the other hand, analyses using nondimensionalization techniques, combined with grid-independence verification and macroscopic energy-balance assessment, have shown that, even with relatively coarse, orthogonal meshes (Jiménez-Islas *et al.*, 2014), the Nusselt number can be computed with high accuracy. These approaches show excellent agreement with previously reported values in the literature and exhibit very low macroscopic energy balance errors (Molina-Herrera *et al.*, 2024). Additionally, comparisons between direct numerical simulation and the *k–ε* model up to Ra = 10^{10} have shown that, although differences in the Nusselt number tend to decrease at very high Rayleigh numbers, the local resolution of the boundary layer, including thermal gradients, pointwise Nusselt number values, and corner vortex formation, is captured more accurately by direct numerical simulation. Furthermore, this approach preserves macroscopic energy balances with greater accuracy, maintaining errors of lower order than those associated with the *k–ε* model (Hernández-López *et al.*, 2016; Igci and Arici, 2016; Cardona *et al.,* 2023; Molina-Herrera *et al.*, 2024). Overall, these results indicate that, at high Rayleigh numbers, boundary-layer-type mesh refinement along the differentially heated walls is crucial for capturing thermal boundary-layer dynamics and accurately describing heat transfer. Within the present scope, the direct numerical solution of the two-dimensional governing equations provides a useful numerical framework for generating benchmark reference data for the classical cavity problem. For these reasons, the aim of this research is to numerically characterize natural convection in the classical differentially heated square cavity at high Rayleigh numbers using direct numerical simulation, defined here as the solution of the two-dimensional incompressible Navier-Stokes equations without turbulence modeling (Orszag, 1970). The study is therefore conceived as a high-resolution numerical benchmark of the De Vahl Davis cavity problem within a two-dimensional framework. To this end, a boundary-layer-type meshing strategy was implemented along the differentially heated walls to accurately resolve the thermal and hydrodynamic boundary layers, using orthogonal, stratified meshes refined near the hot and cold walls. Numerical consistency was verified through grid-independence analysis, macroscopic heat-balance assessment, transient convergence of the wall-integrated Nusselt number, and comparison with reference data from the literature across a broad range of Rayleigh numbers. The specific objectives are to quantify the Nusselt number as a function of the Rayleigh number, analyze the effect of mesh design on wall temperature gradients, and assess the robustness of the predicted heat-transfer behavior in the present two-dimensional formulation. At very high Rayleigh numbers, the results presented here must be interpreted strictly as two-dimensional benchmark solutions of the adopted formulation, not as physically realistic predictions of the fully three-dimensional unsteady cavity flow.

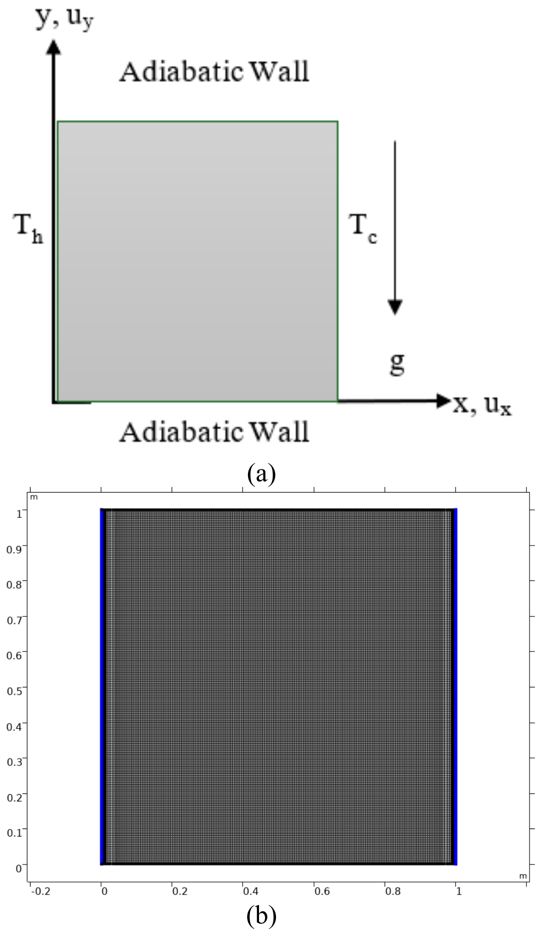

Figure 1. Geometric system. (a) Square cavity with boundary conditions, (b) Orthogonal meshing design with boundary layers (BL) at hot and cold walls.

2 Mathematical model

The problem under study considers a two-dimensional square cavity filled with air, with a side length of L = 1 m. A Cartesian coordinate system is defined, where the x-direction is horizontal (from left to right), and the y-direction is vertical (from bottom to top). At the same time, gravity acts in the negative y-direction. The temperature difference between the vertical walls ($T_h > T_c$) generates density variations that induce a buoyancy-driven recirculating flow. As the imposed temperature difference increases, the flow within the cavity gradually transitions from laminar to turbulent.

The problem is schematically represented in Figure 1, where the square cavity is naturally divided into three flow regions. Along the vertical walls, namely the hot and cold surfaces, thin thermal and hydrodynamic boundary layers develop, where the no-slip condition and the strong temperature contrast generate the most intense velocity and temperature gradients (Henkes and Hoogendoorn, 1989; Xin and

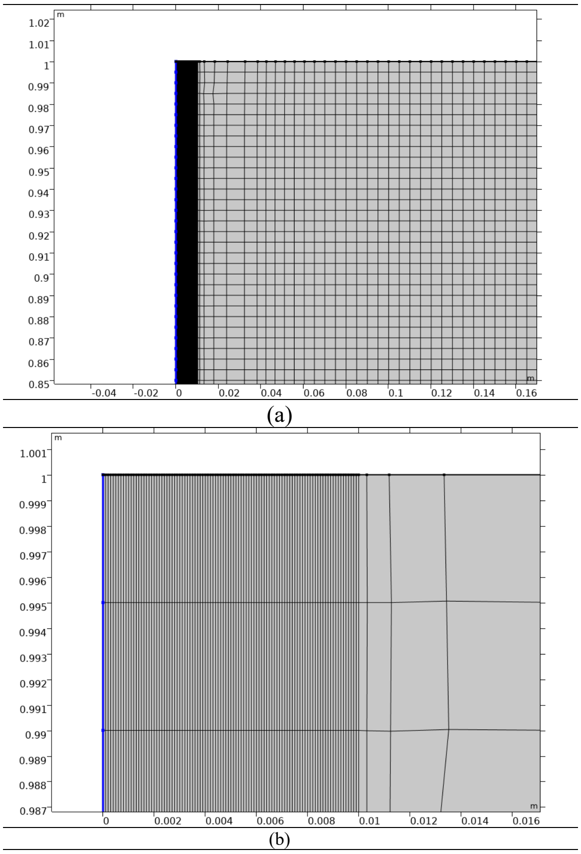

Figure 2. Mesh distribution with two zoom boundary-layer type refinements on the differentially heated cavity.

Le Quéré, 1994). These near-wall regions govern the onset and intensity of buoyancy-driven circulation and determine the local heat-transfer maximum. In contrast, the central region of the domain exhibits smoother fields, characterized by weaker convection and moderate variations of temperature and velocity. Figure 1 illustrates the physical configuration, with the left wall maintained at T_h, the right wall at T_c, and the upper and lower walls treated as adiabatic.

Figure 2 shows the mesh distribution used for the differentially heated cavity. To accurately capture the temperature and velocity gradients in the near-wall regions, a boundary-layer-type mesh was implemented adjacent to the differentially heated walls, thereby ensuring adequate resolution of the thermal and velocity boundary-layer behavior. Within the cavity, a uniform orthogonal discretization was maintained to optimize computational cost without compromising solution stability. Figure 2 shows a two-zoomed view of the region near the differentially heated walls, where the local boundary-layer refinement is evident. This refinement enables a more detailed representation of steep temperature and velocity gradients, as well as the potential formation of vortices or eddies, which are particularly relevant in the high-Rayleigh-number regime.

2.1 *Dimensional governing equations*

To describe momentum and heat transfer within the cavity at steady state, the incompressible Navier-Stokes equations and the energy equation are employed under the Boussinesq approximation (Jiménez-Islas *et al.*, 2009; Bird *et al.*, 2009). Under this approximation, fluid density is assumed to be constant throughout the domain, except in the buoyancy term that models natural convection within the cavity, as presented in Equations (1)-(4) under steady-state conditions (De Vahl Davis, 1983; Henkes and Hoogendoorn, 1989; Molina Herrera *et al.*, 2024). Under these assumptions, physical properties are evaluated at a reference temperature T_0, and the coupling between temperature and momentum occurs exclusively through the buoyancy term, thereby preserving the incompressible formulation of the governing equations. The physical properties of air used in the simulations are summarized in Table 1.

Equations (5a)–(5d) specify the boundary conditions. A no-slip condition ($u_x = u_y = 0$) is imposed on all cavity walls. The vertical walls are differentially heated: the left wall is maintained at T_h and the right wall at T_c, thereby imposing the temperature difference that drives natural convection. The upper and lower walls are treated as adiabatic, enforced by $\partial T/\partial y = 0$, indicating the absence of normal heat flux across these boundaries. These conditions define a closed cavity in which air circulation is driven solely by thermal buoyancy and determine the locations of the maximum thermal gradients within the boundary layers adjacent to the hot and cold walls, respectively (Dorfman and Renner, 2009; Choi and Kim, 2012).

Table 1. Thermodynamic data for air taken from Bird *et al*. (2009).

Variable	Value	Units
Density, ρ	1.177	kg/m^3
Thermal conductivity, k	26.0×10^{-3}	W/m · K
Heat capacity at constant pressure, C_p	1.00×10^{3}	J/kg· K
Volumetric coefficient of thermal expansion, β	3.322×10^{-3}	K^{-1}
Viscosity, μ	1.847×10^{-5}	kg/m· s

2.1.1 Laminar flow model in dimensional variables

$$\frac{\partial u_x}{\partial x} + \frac{\partial u_y}{\partial y} = 0 \tag{1}$$

$$\rho\left(u_x \frac{\partial u_x}{\partial x} + u_y \frac{\partial u_x}{\partial y}\right) = -\frac{\partial p}{\partial x} + \mu\left[\frac{\partial^2 u_x}{\partial x^2} + \frac{\partial^2 u_x}{\partial y^2}\right] \tag{2}$$

$$\rho\left(u_x \frac{\partial u_y}{\partial x} + u_y \frac{\partial u_y}{\partial y}\right) = -\frac{\partial p}{\partial y} + \mu\left[\frac{\partial^2 u_y}{\partial x^2} + \frac{\partial^2 u_y}{\partial y^2}\right] + \rho g \beta (T - T_0) \tag{3}$$

$$\rho c_p\left(u_x \frac{\partial T}{\partial x} + u_y \frac{\partial T}{\partial y}\right) = k\left[\frac{\partial^2 T}{\partial x^2} + \frac{\partial^2 T}{\partial y^2}\right] \tag{4}$$

2.1.2 Boundary conditions

$$B.C.1. \quad x = 0 \quad u_x = u_y = 0 \quad T = T_h \quad 0 \le y \le L \tag{5a}$$

$$B.C.2. \quad x = L \quad u_x = u_y = 0 \quad T = T_c \quad 0 \le y \le L \tag{5b}$$

$$B.C.3. \quad y = 0 \quad u_x = u_y = 0 \quad \partial T/\partial y = 0 \quad 0 \le x \le L \tag{5c}$$

$$B.C.4. \quad y = L \quad u_x = u_y = 0 \quad \partial T/\partial y = 0 \quad 0 \le x \le L \tag{5d}$$

2.2 Dimensionless governing equations

However, solving the Navier–Stokes equations in primitive (dimensional) variables, in both laminar and turbulent regimes, poses significant numerical and physical challenges for natural convection at high Rayleigh numbers, primarily due to scaling and numerical stability issues. When large temperature or velocity differences are present, the terms in the governing equations operate on markedly different orders of magnitude, which promotes round-off errors and loss of accuracy in discretization methods. In addition, iterative algorithms such as the Newton-Raphson method may exhibit convergence difficulties, including increased iteration counts, stagnation, or divergence, hindering the attainment of physically meaningful solutions (Jiménez-Islas *et al.*, 2014). The increased computational cost compounds this difficulty, since working with dimensional variables often requires finer meshes, thereby slowing down the simulations. The problem becomes more pronounced at high Rayleigh numbers, where thermal boundary layers become extremely thin and require very fine meshes to accurately represent temperature and velocity gradients. Finally, result interpretation is further complicated because the numerical values depend on the chosen units, making direct comparison with other studies performed at different scales more difficult.

Nondimensionalization changes the governing variables in dimensionless form, reducing scale disparities among terms and highlighting the relative importance of the dominant transport mechanisms. In the present problem, the Rayleigh and Prandtl numbers characterize the balance among buoyancy, thermal diffusion, and viscosity, and they also facilitate the numerical implementation and conditioning of the algebraic system (Molina Herrera *et al.*, 2024).

Equations (6)–(11d) define the dimensionless laminar model and its associated boundary conditions, enabling the study of natural convection without dependence on specific dimensional scales. From a computational perspective, nondimensionalization enhances numerical stability by eliminating scale disparities among terms in the governing equations, thereby reducing round-off errors and improving computational accuracy. In addition, it yields better-conditioned Jacobian matrices, which promote the convergence of iterative methods such as the Newton-Raphson algorithm (Jiménez-Islas *et al.*, 2014). Furthermore, it facilitates extrapolation and comparison of results, since dimensionless variables are independent of the system of units, enabling direct comparison of theoretical, numerical, and experimental studies conducted under different conditions and allowing solutions to be evaluated without repeating calculations at different physical scales (Molina-Herrera *et al.*, 2024).

2.2.1 Laminar flow model in dimensionless variables

$$\frac{\partial U_x}{\partial X} + \frac{\partial U_y}{\partial Y} = 0 \tag{6}$$

$$U_x \frac{\partial U_x}{\partial X} + U_y \frac{\partial U_x}{\partial Y} = -\frac{\partial p}{\partial X} + \left(\frac{\mathrm{Pr}}{\mathrm{Ra}}\right)^{1/2}\left[\frac{\partial^2 U_x}{\partial X^2} + \frac{\partial^2 U_x}{\partial Y^2}\right] \tag{7}$$

$$U_x \frac{\partial U_y}{\partial X} + U_y \frac{\partial U_y}{\partial Y} = -\frac{\partial P}{\partial Y} + \left(\frac{\mathrm{Pr}}{\mathrm{Ra}}\right)^{1/2}\left[\frac{\partial^2 U_y}{\partial X^2} + \frac{\partial^2 U_y}{\partial Y^2}\right] + \theta \tag{8}$$

$$U_x \frac{\partial \theta}{\partial X} + U_y \frac{\partial \theta}{\partial Y} = \frac{1}{(\mathrm{Pr}\, Ra)^{1/2}}\left(\frac{\partial^2 \theta}{\partial X^2} + \frac{\partial^2 \theta}{\partial Y^2}\right) \tag{9}$$

In Equations (6)–(9), the following variables were introduced.

$$U_x = \frac{u_x}{u_{ref}}; \quad \theta = \frac{T - T_0}{T_1 - T_0}; \quad X = \frac{x}{L};$$
$$(Pr\ Ra)^{1/2} = \frac{\rho L \mathrm{Pr}\, u_{ref}}{\mu}; \quad U_y = \frac{u_y}{u_{ref}};$$
$$u_{ref} = \sqrt{g\beta\Delta T L}; \quad Y = \frac{y}{L}; \quad \left(\frac{\mathrm{Pr}}{Ra}\right)^{1/2} = \frac{\mu}{\rho L u_{ref}} \tag{10}$$

2.2.2 Boundary conditions

$$B.C.1. \quad X = 0 \quad U_x = U_y = 0 \quad \theta = 1 \quad 0 \leq Y \leq 1 \tag{11a}$$

$$B.C.2. \quad X = 1 \quad U_x = U_y = 0 \quad \theta = 0 \quad 0 \leq Y \leq 1 \tag{11b}$$

$$B.C.3. \quad Y = 0 \quad U_x = U_y = 0 \quad \partial\theta/\partial Y = 0 \quad 0 \leq X \leq 1 \tag{11c}$$

$$B.C.4. \quad Y = 1 \quad U_x = U_y = 0 \quad \partial\theta/\partial Y = 0 \quad 0 \leq X \leq 1 \tag{11d}$$

3 Numerical solution

To solve the governing equations of natural convection in the differentially heated cavity under steady-state conditions, the nondimensionalization procedure previously reported by Molina-Herrera *et al.* (2024) was applied. The simulations were performed using COMSOL Multiphysics® version 5.4, installed on a workstation equipped with an Intel Core i9-14900K processor, 64 GB RAM, and Windows 11 Professional. Spatial discretization was performed using the finite element method, a widely used method for the numerical solution of partial differential equations.

The nonlinear solver implemented was the Newton-Raphson method in its automatic form, which iteratively linearizes the coupled system of equations and updates the dependent variables until numerical convergence is achieved within a prescribed tolerance. At each iteration, the algorithm evaluates the Jacobian matrix and applies a successive correction scheme that minimizes the residual error from one iteration to the next. This approach enables the attainment of stable and accurate solutions even at high Rayleigh numbers, where the nonlinearity of the convective terms becomes dominant. It is worth noting that, despite the relatively large number of mesh elements employed, the total computational time for the simulations over the range Ra = 10^3-10^{12} was only 14 minutes, demonstrating the efficiency of the implemented numerical scheme and the robustness of the solution method under fully developed natural-convection conditions. To reach Ra = 10^{12}, a sweeping strategy was adopted, in which the converged solution at a given Rayleigh number was used as the initial guess for the subsequent Rayleigh number, and this procedure was repeated successively.

To solve the differentially heated square-cavity problem, a stratified orthogonal mesh was generated by introducing boundary-layer (BL) regions with a total thickness of 0.01 m along the hot and cold vertical walls (Molina-Herrera and Jiménez-Islas, 2025). The choice of 0.01 m was based on numerical tests performed at Ra = 10^{12}, the most severe case analyzed in this work, for which the near-wall gradients are strongest. Inspection of the corresponding isotherms showed that this BL thickness was sufficient to encompass the full thermal and hydrodynamic boundary-layer structure adjacent to both walls. Figure 3 presents enlarged views of these regions, showing that the near-wall layers are properly resolved within the adopted BL thickness. The remainder of the cavity was discretized using a uniform quadrilateral mesh of 0.005×0.005 m (see Figures 1 and 2). Additional support for this choice is provided by the grid-sensitivity analysis and by the transient verification discussed later, both of which yield Nusselt values consistent with the steady-state predictions.

The impact of boundary-layer-type refinement on the prediction of the dimensionless temperature profile $\theta(X)$ along the cavity centerline was evaluated at Ra = 10^{12}. Figure 4 compares four meshing configurations applied to the differentially heated walls: BL = 80, BL = 100, BL = 120, and an extreme case with BL = 1000. The results show that, starting from BL = 100, the θ profile at the cavity center remains almost unchanged, and the temperature profiles with BL = 100 and BL = 120 nearly overlap. This indicates that further refinement does not significantly alter the temperature profile across the domain. These findings confirm that a mesh with 100 boundary-layer-type layers is sufficient to resolve the wall-normal gradients associated with the ultrafine boundary layers that develop along the differentially heated walls at Ra = 10^{12}, without causing numerical errors in the near-wall regions (Henkes and Hoogendoorn, 1989; Xin and Le Quéré, 1994; Trias *et al*., 2007; Igci and Arici, 2016).

Mesh quality was assessed for the reference quadrilateral mesh with 100 boundary-layer elements per vertical wall (BL = 100), which was used in both steady-state and transient simulations. The complete mesh consists of 80,000 quadrilateral elements and 80,601 vertices. According to the COMSOL mesh statistics, the minimum element quality was 0.9136, and the average was 0.9998, indicating that even the least favorable elements remain high quality. The core region was discretized with a uniform mesh of 0.005×0.005 m and a maximum element growth rate of 1, which confirms a fully regular mesh in the interior of the cavity. These metrics indicate that the adopted mesh does not contain degenerate or highly distorted elements that could compromise numerical conditioning or the predicted Nusselt numbers. The resulting nonlinear algebraic system was solved in COMSOL using the automatic Newton method within a fully coupled formulation. The iterative process began with an initial damping factor of 0.01, after which the solver automatically adjusted it to improve robustness to convergence. A relative tolerance of 0.005 was used, and the linearized systems arising at each Newton step were solved with a direct solver within the fully coupled scheme. These settings provided stable convergence over the range of Rayleigh numbers considered in the present study.

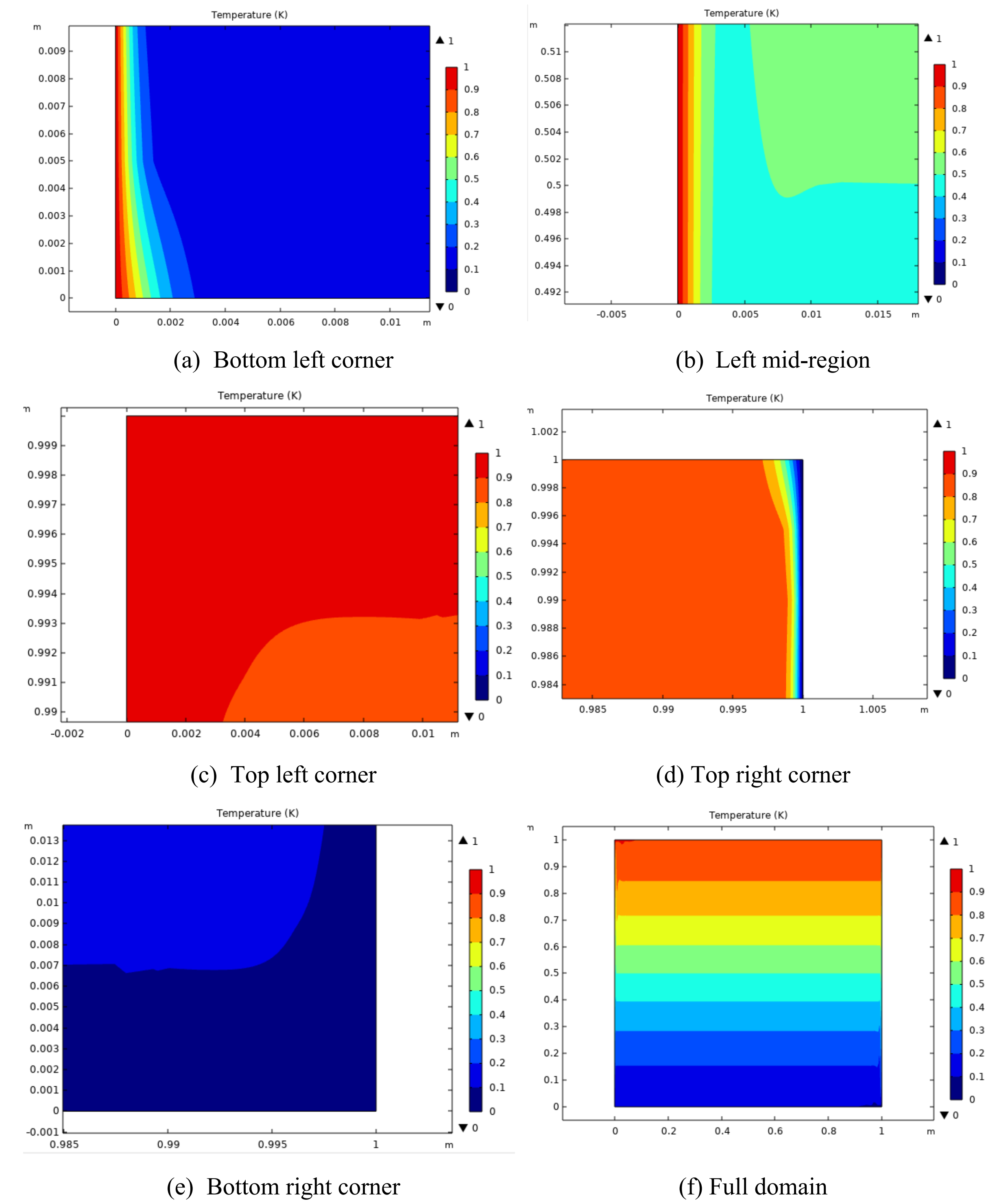

(a) Bottom left corner

(b) Left mid-region

(c) Top left corner

(d) Top right corner

(e) Bottom right corner

(f) Full domain

Figure 3. Enlarged views of the near-wall regions at Ra = 10^{12}, showing the boundary-layer mesh of total thickness 0.01 m along the hot and cold vertical walls. The figure illustrates that the thermal and hydrodynamic boundary-layer structure is fully contained within the adopted BL region.

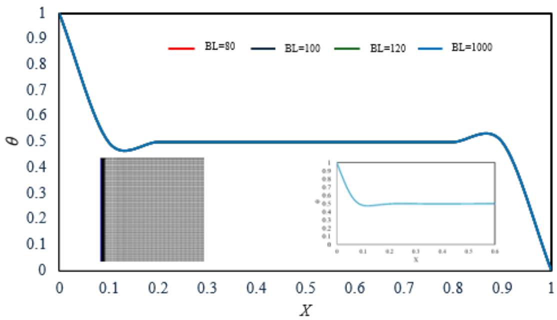

Figure 4. Dimensionless temperature profiles along the cavity centerline for different boundary-layer-type refinements at Ra = 10^{12}.

As an additional verification step, the BL = 1000 case was included, which represents an extremely fine discretization near the boundaries. This configuration reproduces the temperature profile almost identically to that obtained with the BL = 100 and BL = 120 meshes, thereby confirming that the solution has reached the grid-independent regime. However, because increasing BL to 1000 scales computational cost proportionally and may adversely affect numerical stability, the BL = 100 configuration was selected as the best compromise between accuracy and computational efficiency, ensuring precise results with reasonable runtime. Based on these findings, Table 2 presents the effect of boundary-layer-type refinement on the Nusselt number over a wide range of Rayleigh numbers, for different meshing configurations characterized by the total number of elements in the domain and the number of elements concentrated along the differentially heated walls. The results demonstrate that adequate resolution of the thermal boundary layers is the determining factor in achieving numerically consistent solutions, particularly in the high-Rayleigh-number regime considered within the present two-dimensional formulation (Ra $\geq 10^{10}$).

Table 2 also shows the configurations with BL = 20 and BL = 40. However, they converge for moderate Rayleigh numbers but do not achieve numerical convergence for Ra = 10^{12}, as evidenced by the absence of results in the table. This behavior indicates that the discretization is unable to adequately resolve the ultrathin temperature gradients that develop near the differentially heated walls at extreme Rayleigh numbers, leading to numerical instability when attempting to reach a steady-state solution. In contrast, convergence is achieved from BL = 60 onward for Ra = 10^{12}, demonstrating that a minimum level of refinement in the wall-normal direction along the differentially heated walls is indispensable for adequately resolving the steep near-wall gradients of the adopted two-dimensional formulation as the number of boundary-layer-type layers is increased from BL = 60 to BL = 120, the Nusselt number values for Ra $\geq 10^{10}$ exhibit a clear tendency toward converged values, with progressively smaller variations between consecutive mesh configurations.

For Ra = 10^{12}, the relative difference in the Nusselt numbers obtained with BL = 80, 100, and 120 is below 0.1%, confirming that the solution is grid-independent with respect to boundary-layer refinement. This behavior is consistent with the flow physics, since once the thermal and hydrodynamic boundary layers are adequately resolved, further mesh refinement does not produce appreciable changes in the global heat transfer.

To independently verify this converged behavior, an extreme case with BL = 1000 was considered, corresponding to an extremely fine discretization along the differentially heated walls. The results obtained with this configuration reproduce essentially the same Nusselt number values as those from the BL = 100 and BL = 120 cases, indicating that the numerical solution no longer depends on additional mesh refinement. However, this increase in boundary-layer resolution along the differentially heated walls entails a significant increase in computational time,

Table 2. Impact of Boundary Layers (BL) on Nusselt Number at Various Rayleigh Numbers, at tolerance = 0.005.

Elements in the whole domain	48,000	56,000	64,000	72,000	80,000	88,000	440,000
Elements in the Boundary Layer	880	960	1,040	1,120	1,200	1,280	4,800
Ra	BL = 20	BL = 40	BL = 60	BL = 80	BL = 100	BL = 120	BL = 1000
10^3	1.1178	1.1178	1.1178	1.1177	1.1178	1.1178	1.1177
10^4	2.2448	2.2448	1.1178	2.2448	2.2448	2.2448	2.2448
10^5	4.5215	4.5214	4.5213	4.5213	4.5212	4.5212	4.5210
10^6	8.8258	8.8252	8.8249	8.8248	8.8246	8.8245	8.8232
10^7	16.539	16.542	16.544	16.545	16.546	16.547	16.550
10^8	30.270	30.278	30.282	30.285	30.289	30.293	30.341
10^9	54.479	54.473	54.474	54.479	54.485	54.491	54.512
10^{10}	97.637	97.634	97.62	97.615	97.613	97.612	97.621
10^{11}	173.91	174.33	174.33	174.32	174.32	174.31	174.07
10^{12}	NC	NC	309.07	309.03	308.95	308.85	308.25
CPU Time (minutes)	4.450 5.419x10^{11*}	6.167 8.966x10^{11*}	14.233	13.850	14.000	15.383	128.483

*Maximum value obtained for the Ra number.

Table 3. Temporal statistics of the wall-integrated Nusselt number obtained from transient 2-D simulations using the reference mesh with BL=100.

Rayleigh number	Final time-lapse	<Nu> at X = 0	σ at X = 0	CV (%) at X=0	<Nu> at X = 1	σ at X = 1	CV (%) at X = 1	Mean relative difference between walls (%)
10^{10}	3000–5000	98.247	0.251	0.256	98.326	0.251	0.255	0.268
10^{11}	3000–5000	174.487	0.034	0.019	174.451	0.038	0.022	0.030
10^{12}	10000–12000	309.163	0.003	0.001	309.147	0.011	0.004	0.005

Note: The transient simulations were carried out using the same quadrilateral reference mesh employed in the steady-state calculations, with BL=100. The coefficient of variation was computed as CV = 100 σ <Nu>, where <Nu> is the average Nusselt number in the final time-lapse.

from approximately 14–15 minutes for BL = 100–120 to more than 120 minutes for BL = 1000, without yielding a proportional improvement in the accuracy of the results. Therefore, these results confirm that a BL = 100 configuration provides an optimal balance between numerical accuracy, computational stability, and computational cost, enabling numerically robust estimation of the Nusselt number within the present two-dimensional framework. As a further mesh-sensitivity check, a refined quadrilateral mesh was tested with a core mesh size of 0.004×0.004 m and 200 boundary-layer elements, distributed over the same total BL thickness of 0.01 m. For this refined discretization, the wall-integrated Nusselt numbers were Nu = 310.7202 at the hot wall (X=0) and Nu = 310.7201 at the cold wall (X=1), showing practically identical values at both boundaries. Since this result differs only slightly from that obtained with the reference mesh, the additional test further confirms that the predicted heat-transfer rate is practically insensitive to further mesh refinement within the present two-dimensional framework.

3.1 *Transient verification of the steady-state Nusselt number*

As an additional validation metric beyond grid independence and macroscopic heat-balance verification, transient simulations were conducted for Ra = 10^{10}, 10^{11}, and 10^{12} using the same reference mesh used in the steady-state calculations, specifically the quadrilateral mesh with BL=100. The wall-integrated Nusselt number was monitored over time, and the corresponding temporal statistics are presented in Table 3. Figure 5 shows that, in all cases, the transient response exhibited an initial relaxation stage followed by a quasi-stationary regime. The long-time mean values at the hot wall (X = 0) were Nu = 98.247, 174.487, and 309.163 for Ra = 10^{10}, 10^{11}, and 10^{12}, respectively, with very small temporal fluctuations in the final stage. As also shown in Table 3, the differences between the hot- and cold-wall integrated Nusselt numbers remained very small in the final regime. These results demonstrate that the steady-state Nusselt values reported in this work are consistent

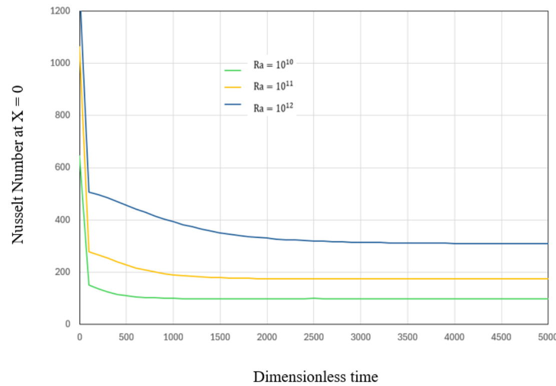

Figure 5. Time evolution of the wall integrated Nusselt number at the hot wall (X=0) for Ra = 10^{10}, 10^{11}, and 10^{12}.

with the long-time asymptotic limit of the same two-dimensional formulation. In addition, the increase in the settling time with the Rayleigh number reflects the greater numerical stiffness of the problem at high Ra.

4 Results and discussion

This section presents an analysis of dimensionless numerical solutions for the two-dimensional differentially heated square cavity over the Rayleigh-number range $10^3 \leq Ra \leq 10^{12}$. The results are organized into several subsections to provide a comprehensive assessment of the adopted formulation. First, the Nusselt number serves as a reference for benchmarking heat-transfer behavior. Subsequently, the macroscopic energy balance is examined to assess the numerical consistency of the simulations. In addition, temperature contours and streamlines are presented to describe the thermal structure and flow patterns within the cavity. Finally, the temperature and velocity profiles are analyzed to provide a detailed characterization of boundary-layer evolution and convective behavior in this two-dimensional framework. At the highest Rayleigh numbers, these results are interpreted as benchmark solutions for the adopted 2-D formulation.

Table 4. Comparison of the Nusselt number computed in the present study using the present 2-D finite-element formulation with values reported by other authors.

Ra	Nu Dixit *et al*. (2006)	Nu Goloviznin *et al*. (2016)	Nu This Work
10^3	1.122	1.117	1.1178
10^4	2.28	2.236	2.2448
10^5	4.54	4.516	4.5212
10^6	8.65	8.822	8.8246
10^7	16.79	16.63	16.546
10^8	31.5	30.3	30.289
10^9	57.3	55.6	54.485
10^{10}	103.67	100.3	97.613
10^{11}	NA	174	174.32
10^{12}	NA	367	308.95

4.1 *Nusselt number*

From a practical perspective, the Nusselt number is the key metric for evaluating heat transfer efficiency in convection. Being dimensionless, it compares the total heat transfer (convection plus conduction) with that which would occur solely by conduction if the fluid were at rest; thus, it quantifies the enhancement of heat transport due to convective motion.

In differentially heated cavities, the Nusselt number is a direct quantitative measure of the convective intensity driven by temperature gradients, with higher values typically associated with thinner thermal boundary layers and, consequently, stronger heat fluxes. Due to its sensitivity to boundary-layer resolution and boundary conditions, the Nusselt number is an essential parameter for validating numerical simulations, including direct numerical solution of the governing equations, Reynolds-Averaged Navier-Stokes models, and Large Eddy Simulation, as well as for assessing grid independence and verifying the macroscopic energy balance. In practice, the Nusselt number is defined as Nu = hL/k, where h is the convective heat-transfer coefficient, L is a characteristic length, and k is the thermal conductivity. Alternatively, it can be defined locally in terms of the temperature gradient normal to the wall. In this study, the Nusselt number for a square cavity with differentially heated vertical walls is determined as described below.

$$\overline{Nu} = \int_0^1 -\frac{\partial\theta}{\partial X}\bigg|_{X=0} dY \tag{12}$$

To assess the accuracy of the temperature and velocity profiles obtained using the proposed numerical solution of the two-dimensional governing equations, the Nusselt number was compared with reference values reported in the literature (Dixit and Babu, 2006; Goloviznin *et al.*, 2016). Table 4 compares the Nusselt numbers computed in the present study using 2-D numerical simulation with a BL = 100 mesh with those previously reported by Dixit and Babu (2006) and Goloviznin *et al.* (2016) for the differentially heated square cavity over a wide range of Rayleigh numbers. The results show good agreement among the three studies, particularly in the laminar and transitional flow regimes ($10^8 \leq$ Ra $\leq 10^{10}$), which confirms that the meshing strategy adopted in this work adequately resolves temperature gradients and ensures grid independence of the reported Nusselt number values. Within the Rayleigh number range covered by Dixit and Babu (2006), the values obtained in this study reproduce both the increasing trend of the Nusselt number and the previously reported global magnitudes, with moderate discrepancies attributable to differences in numerical methods, discretization schemes, and convergence criteria. This level of agreement reinforces that boundary-layer-type refinement with BL = 100 is sufficient to reproduce the benchmark behavior of the adopted two-dimensional cavity formulation up to high Rayleigh numbers.

For higher Rayleigh numbers, where the available reference data correspond to Goloviznin *et al.* (2016), the results of the present study continue to exhibit stable, converged behavior. These solution characteristics are independent of further mesh refinement. In particular, the agreement observed for Ra $\leq 10^{11}$ confirms that the employed mesh adequately resolves the ultrafine boundary layers. Although a more noticeable difference is observed for Ra = 10^{12} compared with the available reference, the grid-independence analysis confirms that this variation cannot be attributed to insufficient resolution of the thermal boundary layers but rather to methodological differences between the numerical schemes employed.

Therefore, the comparison presented in Table 4, together with the detailed convergence and boundary-layer-type refinement study (see Table 2), confirms that the mesh with BL = 100 provides results that are independent of additional mesh refinement, numerically robust, and comparable with both classical and contemporary references for benchmark

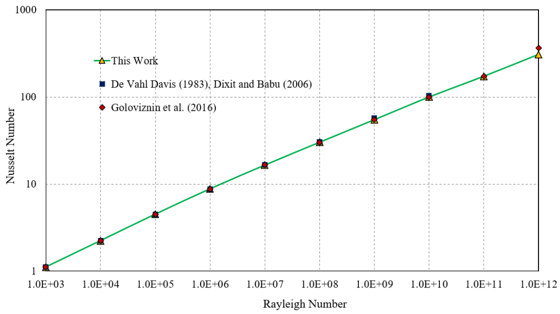

Figure 6. Comparison of the Nusselt number computed in this study with classical and modern reference data from De Vahl Davis (1983), Dixit and Babu (2006), and Goloviznin *et al*. (2016).

evaluation of the Nusselt number within the current two-dimensional framework. Figure 6 compares the Nusselt numbers obtained in the present study using BL=100 with classical and modern reference data for the differentially heated square cavity. Overall, the figure shows very good agreement with the results of De Vahl Davis (1983) and Dixit and Babu (2006) over the Rayleigh-number range covered by those studies. This agreement supports the accuracy of both the numerical formulation and the adopted boundary-layer-type refinement strategy for capturing heat transfer as the Rayleigh number increases. When the comparison is extended to the data of Goloviznin *et al*. (2016), Figure 6 shows that the overall Nu-Ra trend remains consistent up to high Rayleigh numbers (Ra $\leq 10^{11}$). However, at Ra = 10^{12}, a noticeable difference appears, with Goloviznin *et al.* (2016) reporting a higher Nusselt number than that obtained in the present study. This difference should be interpreted in light of the mesh-sensitivity, convergence, and transient-verification analyses presented previously, which show that the results obtained with BL= 100 remain practically unchanged under further refinement and are consistent with the long-time asymptotic behavior of the same two-dimensional formulation. In addition, an empirical power-law regression of the computed Nusselt numbers over the range $10^3 \leq$ Ra $\leq 10^{11}$ yields Nu = 0.3017Ra$^{0.2508}$. Extrapolation of this correlation to Ra = 10^{12} gives Nu $\approx$ 308.7, which is in excellent agreement with the values obtained from the steady and transient simulations (308.26 and 309.16, respectively). This result indicates that the high-Rayleigh-number prediction remains consistent with the overall Nu-Ra scaling behavior of the present two-dimensional numerical dataset.

An extreme case with BL = 1000 was evaluated explicitly as a validation test, reproducing Nusselt number values essentially identical to those of the BL = 100 and BL = 120 configurations, thereby confirming that the solution does not depend on additional wall-mesh refinement (see Table 2).

Table 5 compares the Nusselt numbers obtained in this study with those reported by various authors over the range $10^3 \leq$ Ra $\leq 10^{12}$, together with the numerical method employed in each case, including finite differences, finite volumes, finite elements, lattice Boltzmann methods, and CABARET schemes, among others. In the low-to-intermediate range (10^3–10^6), the computed values show remarkable agreement with the classical results of De Vahl Davis (1983), indicating that the numerical implementation accurately reproduces the reference laminar solution and that the imposed boundary conditions and spatial

Table 5. Comparison of the average Nusselt number calculated using the present 2-D numerical formulation versus those reported by other authors.

Authors	10^3	10^4	10^5	10^6	10^7	10^8	10^9	10^{10}	10^{11}	10^{12}
De Vahl Davis (1983). Finite Difference Method	1.50	3.52	4.51	8.79	NA	NA	NA	NA	NA	NA
Markatos and Pericleous (1984). Finite volume approach	3.54	3.48	4.43	8.7	NA	32.0	NA	156.8	137.5	840.13
Barakos *et al.* (1994*)*. Finite-Domain Equations	1.11	2.24	4.51	8.81	NA	30.1	54.4	97.6	134.6	NA
Dixit and Babu, (2006). Lattice Boltzmann method	1.12	2.28	4.54	8.65	16.79	30.5	57.3	103.6	NA	NA
Goloviznin *et al.* (2016). CABARET scheme	1.17	2.23	4.51	8.82	NA	30.3	55.6	100.3	174	367
Hernández-López *et al.* (2016). Lattice Boltzmann method	1.11	2.24	4.45	8.86	NA	NA	58.0	137.7	318.53	725.57
Molina-Herrera *et al.* (2024). Orthogonal collocation method	1.11	2.24	4.51	8.82	16.51	30.2	NA	NA	NA	NA
Molina-Herrera and Jiménez-Islas (2025). Finite Element Method	1.12	2.24	4.52	8.83	16.53	30.23	54.89	100.01	NA	NA
This work Finite Element Method	1.12	2.25	4.52	8.82	16.55	30.29	54.89	97.61	174.32	308.95
Nusselt number using the Orthogonal Collocation Method.	1.11	2.24	4.51	8.80	16.48	30.13	54.31	NA	NA	NA

resolution are adequate for capturing the thermal behavior of the flow (Markatos and Pericleous, 1984; Barakos *et al.*, 1994; Welti-Chanes *et al.,* 2005; Dixit and Babu, 2006; Hernández-López *et al.*, 2016).

In the intermediate-to-high range (10^7–10^9), Nusselt numbers exhibit minor variations across studies, mainly attributable to differences in numerical methods, spatial resolution, and convergence criteria. However, in the range 10^{10}–10^{11}, the results obtained in this work show excellent agreement with previously reported values, thereby confirming the accuracy of the numerical simulations. This level of numerical and physical consistency is primarily associated with the use of a boundary-layer-type refined mesh along the differentially heated walls, which enables a detailed description of the steep gradients within the thermal and velocity boundary layers. As a result, an accurate resolution of the corresponding 2-D thermal and flow fields is achieved even at high Rayleigh numbers within the adopted formulation (Henkes and Hoogendoorn, 1989; Xin and Le Quéré, 1994; Goloviznin *et al.*, 2016; Hernández-López *et al.*, 2016; Castillo and Henríquez, 2017).

By extending the analysis to the extreme regime of Ra = 10^{12}, the results of the present study maintain a trend consistent with the evolution observed at high Rayleigh numbers, exhibiting a sustained increase in the Nusselt number associated with the progressive thinning of the thermal boundary layers. Although more noticeable differences with respect to some previous studies are observed in this regime, these discrepancies should be interpreted considering methodological differences among the approaches employed, particularly in the temporal treatment of the problem and the discretization strategy. In this work, the steady-state solution obtained for Ra = 10^{12} was verified through a detailed mesh-refinement study, including an extreme case with a significantly larger number of boundary-layer-type layers, which confirmed that the reported values are independent of further mesh refinement. Consequently, the results presented for Ra = 10^{12} can be considered numerically robust within the adopted two-dimensional framework, extending the available benchmark dataset for the 2-D cavity formulation, and reinforcing the capability of the employed numerical approach to characterize the corresponding two-dimensional problem at high Rayleigh numbers.

Finally, to independently validate the results, the differentially heated square cavity problem was also solved using the orthogonal collocation method with Legendre polynomials and the NEWCOL2L code (FORTRAN 90). The discretized system was solved using a modified Newton-Raphson method with LU factorization, and the Jacobian's partial derivatives were approximated using finite differences. Within this framework, mesh sizes of 51 × 51 nodes already yield grid-independent results (Jiménez-Islas *et al.*, 2014). However, to reach Ra = 10^9, a collocation mesh of 71 × 71 points was required.

Table 6. Comparison of the percentage error of the Nusselt number computed using the finite element method and the orthogonal collocation method.

Ra	FEM	OCM	Error (%)
10^3	1.1178	1.10	0.90
10^4	2.2448	2.24	0.00
10^5	4.5212	4.52	0.22
10^6	8.8246	8.80	0.33
10^7	16.546	16.48	0.48
10^8	30.289	30.13	0.59
10^9	54.485	54.31	0.47
10^{10}	97.613	NA	NA
10^{11}	174.32	NA	NA
10^{12}	308.95	NA	NA

Table 6 compares Nusselt numbers computed using the finite volume and orthogonal collocation methods up to Ra = 10^9, showing percentage errors below 1% in all cases, with 0.33% at Ra = 10^6 and 0.59% at Ra = 10^8. These results indicate that, despite using different discretization approaches, both methods capture the wall-normal gradients and, consequently, the average Nusselt number with comparable accuracy. This level of agreement supports the suitability of stratified and orthogonal meshing near the hot and cold walls for resolving boundary layers. Overall, this comparison suggests minimal numerical bias over the range $10^3 \leq$ Ra $\leq 10^9$ and establishes a reliable basis for extending the analysis to progressively higher Rayleigh numbers.

4.2 Macroscopic energy balance

Another criterion for validating the numerical method is to compute the percentage error in the macroscopic energy balance for a two-dimensional square cavity with adiabatic upper and lower walls, as illustrated in Figure 7. Analysis of this balance constitutes a fundamental verification of simulation quality, since it allows direct evaluation of thermal energy conservation within the computational domain. Under these boundary conditions, the macroscopic energy balance requires that the convective heat flux from the hot wall to the fluid equals the heat leaving the domain through the cold wall. Any discrepancy between these two quantities is interpreted as a measure of the global model error.

In addition, the adiabatic condition imposed on the upper and lower horizontal walls requires that the heat flux across these boundaries be zero or near zero. Consequently, noticeable deviations in these regions would reveal potential limitations in spatial discretization or inconsistencies in numerical

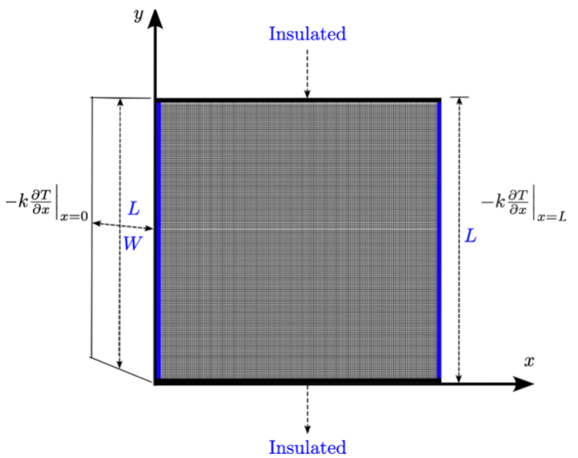

Figure 7. Geometric system for macroscopic energy balance.

Table 7. Comparison of the global macroscopic energy balance computed using the finite volume method and the orthogonal collocation method (OCM).

Ra	FEM	OCM
10^3	0.00	6.028×10^{-6}
10^4	0.00	1.028×10^{-5}
10^5	0.00	1.20×10^{-5}
10^6	0.00	1.46×10^{-5}
10^7	0.00	1.79×10^{-5}
10^8	1.00×10^{-6}	1.79×10^{-5}
10^9	1.00×10^{-6}	2.20×10^{-5}
10^{10}	1.00×10^{-5}	NA
10^{11}	1.03×10^{-6}	NA
10^{12}	6.88×10^{-2}	NA

resolution. Taken together, these checks ensure global conservation of thermal energy within the cavity and, therefore, the reliability of the computed Nusselt numbers (Molina-Herrera and Jiménez-Islas, 2025). The verification was carried out by quantifying the net heat flux across all walls using Equations (13)–(15), thereby enabling the evaluation of the percentage error in the energy balance for each Rayleigh number considered.

$$Q_{In} = \int_0^W \int_0^L \left(-k \left.\frac{\partial T}{\partial x}\right|_{x=0}\right) dydz + \int_0^W \int_0^L \left(-k \left.\frac{\partial T}{\partial y}\right|_{y=0}\right) dxdz \quad (13)$$

$$Q_{Out} = \int_0^W \int_0^L \left(-k \left.\frac{\partial T}{\partial x}\right|_{x=L}\right) dydz + \int_0^W \int_0^L \left(-k \left.\frac{\partial T}{\partial y}\right|_{y=L}\right) dxdz \quad (14)$$

$$\%\ error = \left| \frac{Q_{In} - Q_{Out}}{Q_{In}} \right| \times 100 \quad (15)$$

To validate the model's physical and numerical accuracy at high Rayleigh numbers, the macroscopic energy balance was computed as a function of Rayleigh number using two numerical approaches. Accordingly, Table 7 compares the macroscopic energy balances obtained from the numerical strategy using the finite element method with an orthogonal mesh refined along the differentially heated walls, with those obtained using an independent orthogonal collocation method.

The results show that, for the numerical strategy based on the finite element method with an orthogonal refined mesh along the differentially heated walls, the macroscopic energy balance remains practically zero up to Ra $\leq 10^7$. This behavior validates the results presented in this work by confirming macroscopic energy conservation and adequate resolution of the boundary layers. However, from Ra = 10^8 onward, the macroscopic energy balance obtained with two-dimensional numerical simulations remains on the order of 10^{-3}, reaching a maximum value of 6.38×10^{-2} at Ra = 10^{12}. Even under the highest Rayleigh-number conditions considered in the present two-dimensional formulation, this value remains low and admissible from an energy-conservation standpoint, and it does not compromise the validity of the reported results.

On the other hand, the orthogonal collocation method with a 71 × 71 node mesh yields energy balances close to zero over the range $10^3 \leq$ Ra $\leq 10^9$, thereby verifying the numerical consistency of the model within this interval. However, extending the orthogonal collocation method to Ra $\geq 10^{10}$ was not pursued due to the increased requirements for spatial resolution and numerical stability imposed by this regime, which would have demanded computational time and processing resources not available at the current stage of the study. Overall, both approaches support the numerical consistency of the results, demonstrating that a two-dimensional finite-element numerical simulation with refined meshing adequately reproduces energy conservation under the high-Rayleigh-number conditions analyzed in this study.

4.3 Temperature contours and stream function

Figure 8 presents the temperature contours for high Rayleigh numbers (Ra = 10^9–10^{12}). Within this range, energy transport is fully dominated by natural convection. At the same time, conduction prevails only within the very thin heat transfer boundary layers adjacent to the differentially heated walls, where the maximum temperature gradients are concentrated. For Ra = 10^9, the core region retains an almost uniform energy distribution, with predominantly horizontal isotherms and weak recirculation confined near the

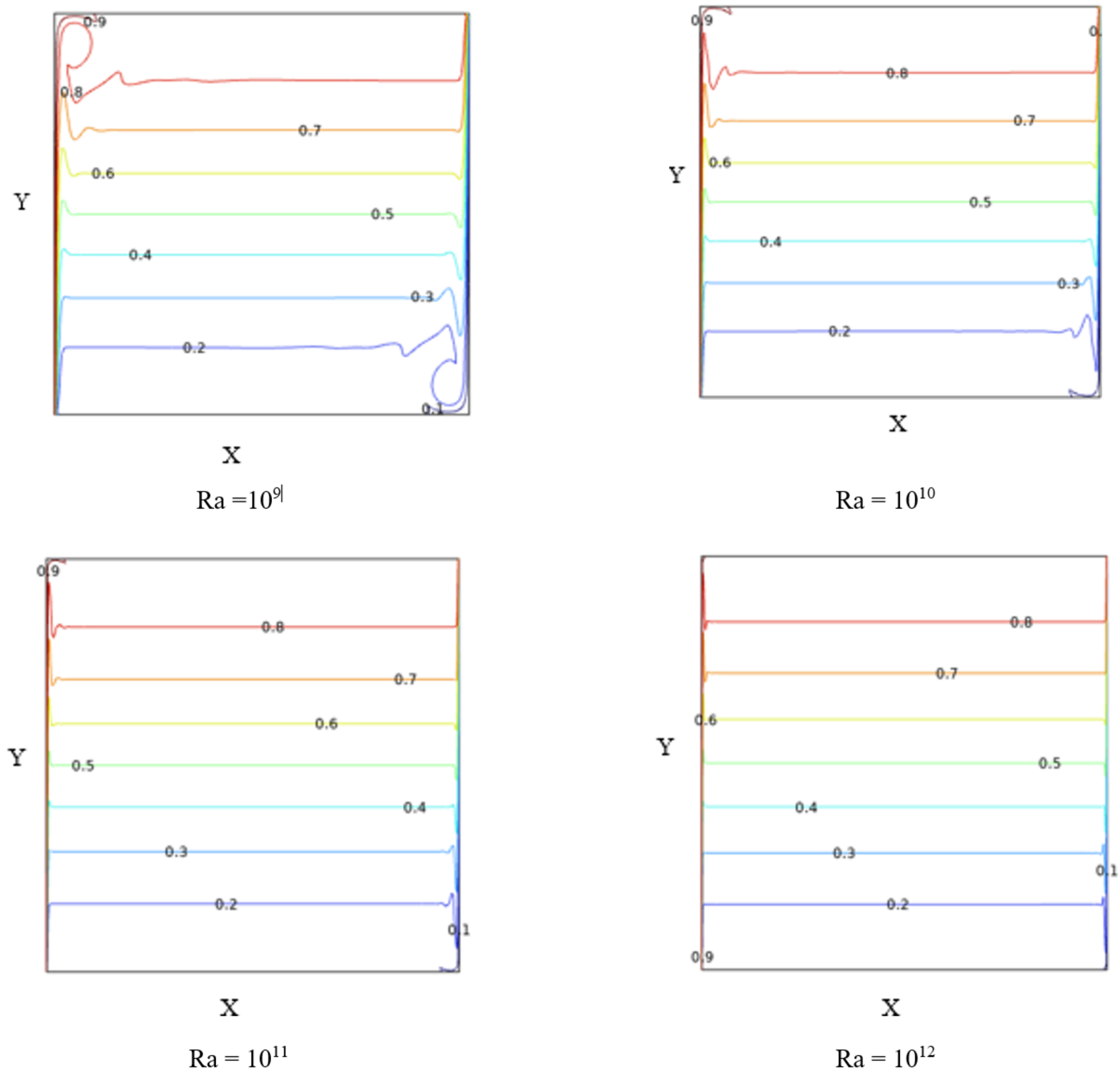

Figure 8. Isotherms for high Rayleigh numbers.

corners. At Ra = 10^{10}, the temperature uniformity within the core increases significantly. The isotherms become nearly parallel to the hot and cold vertical walls, indicating a well-defined downward flow along the hot wall and an upward flow along the cold wall, where the largest temperature gradients are located (Dixit and Babu, 2006; Hernández-López *et al.*, 2016).

Figure 9 shows the stream function contours for high Rayleigh numbers (Ra = 10^9–10^{12}). In all cases, a dominant counterclockwise circulation cell is observed, driven by an upward flow adjacent to the hot wall on the left and a downward flow along the cold wall on the right, a characteristic of natural convection in square cavities. For Ra = 10^9, the pattern exhibits a well-defined primary cell and secondary vortices located at the upper-left and lower-right corners. The streamlines are nearly horizontal in the core region, reflecting a stable flow with moderate velocity gradients. As the Rayleigh number increases to Ra = 10^{10}, the corner recirculation becomes compressed, and the core flow becomes more unidirectional, with long, nearly parallel trajectories, indicating that convection dominates throughout the domain (Dixit and Babu, 2006; Hernández-López *et al.*, 2016). At Ra = 10^{11}, the primary circulation intensifies and becomes further concentrated near the differentially heated walls, while the core region maintains a more uniform flow pattern.

The secondary vortices persist, although they are smaller and confined to the corner regions (Markatos and Pericleous, 1984; Barakos *et al.*, 1994; Hernández-López *et al.*, 2016; Goloviznin *et al.*, 2016). Finally, at Ra = 10^{12}, the flow exhibits highly intensified convection within the adopted two-dimensional formulation, with very intense crossflows near the corners. The secondary cells are confined to very small regions, and the core exhibits an almost uniform streamfunction distribution, indicating that transport is entirely dominated by convection (Hernández-López *et al.*, 2016; Goloviznin *et al.*, 2016). It is also important to note that results for $10^3 \leq$ Ra $\leq 10^8$ were reported in previous studies by Molina-Herrera *et al.* (2024) and Molina-Herrera and Jiménez-Islas (2025), where the transition from the conductive regime to fully developed convection is described in detail.

Figure 10 illustrates the vortex dynamics in the upper-left region of the cavity, corresponding to the hot wall, for $10^9 \leq$ Ra $\leq 10^{12}$. The arrows indicate the local flow direction. The figures show that as the Rayleigh number increases, the corner vortices evolve from broad, smooth recirculation zones into compact, multiple structures confined within progressively thinner boundary layers. In contrast, the flow outside the corner region becomes predominantly unidirectional. This behavior is fundamental, as regions of intense recirculation and steep velocity gradients generate local maxima in $\partial T/\partial X$, thereby directly contributing to accurate Nusselt number predictions. Consequently, turbulence models based on the Reynolds-Averaged Navier-Stokes framework tend to underestimate these small-scale structures at high Rayleigh numbers, which reinforces the need to employ two-dimensional numerical simulation with boundary-layer-type refinement to faithfully reproduce the vortical structures in the upper and lower corners of the cavity (Pérez-Segarra *et al.*, 1995; Duchaine, 2010; Igci and Arici, 2016; Molina-Herrera and Jimenez-Islas, 2025).

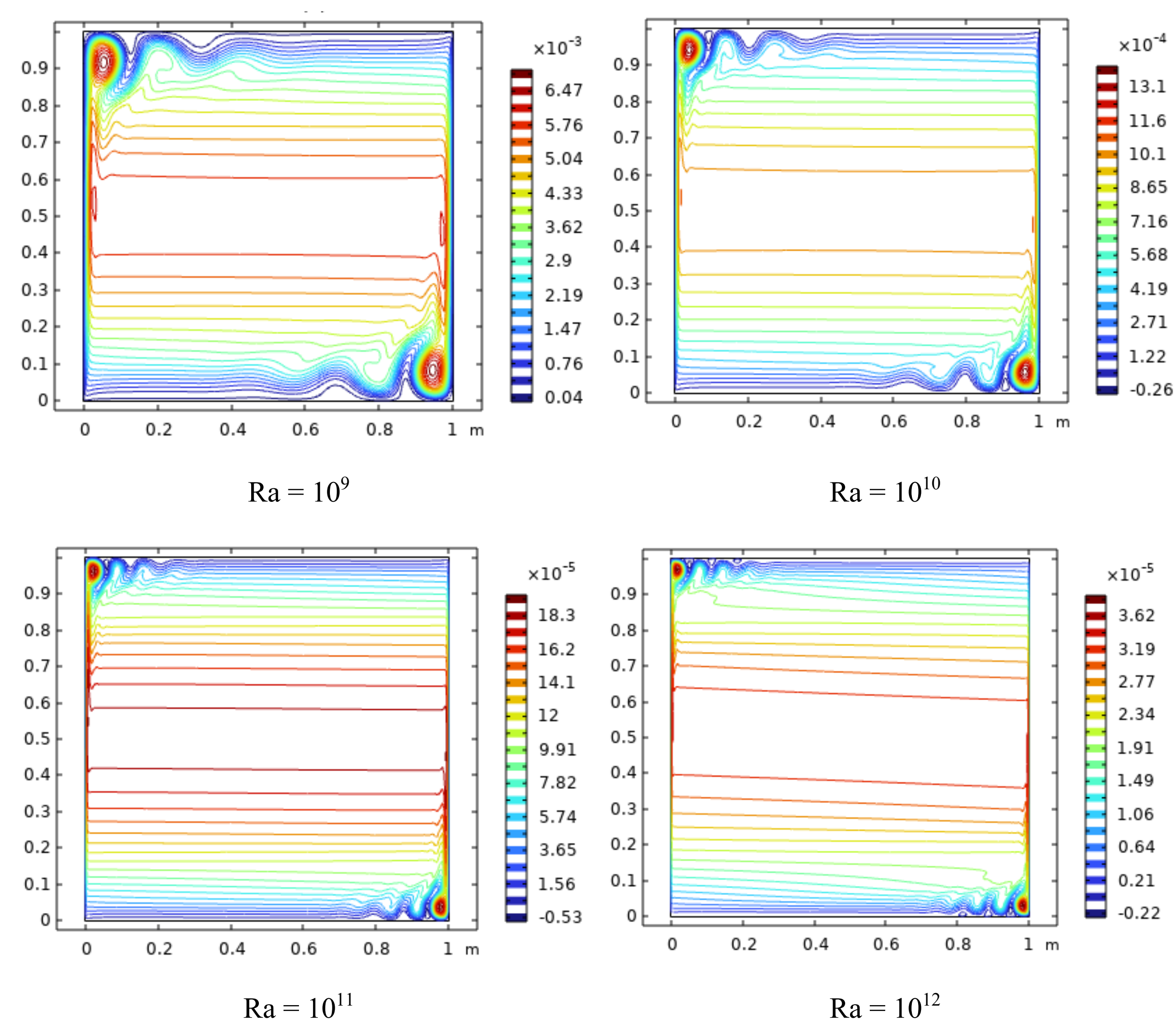

Figure 9. Dimensionless streamlines for high Rayleigh numbers.

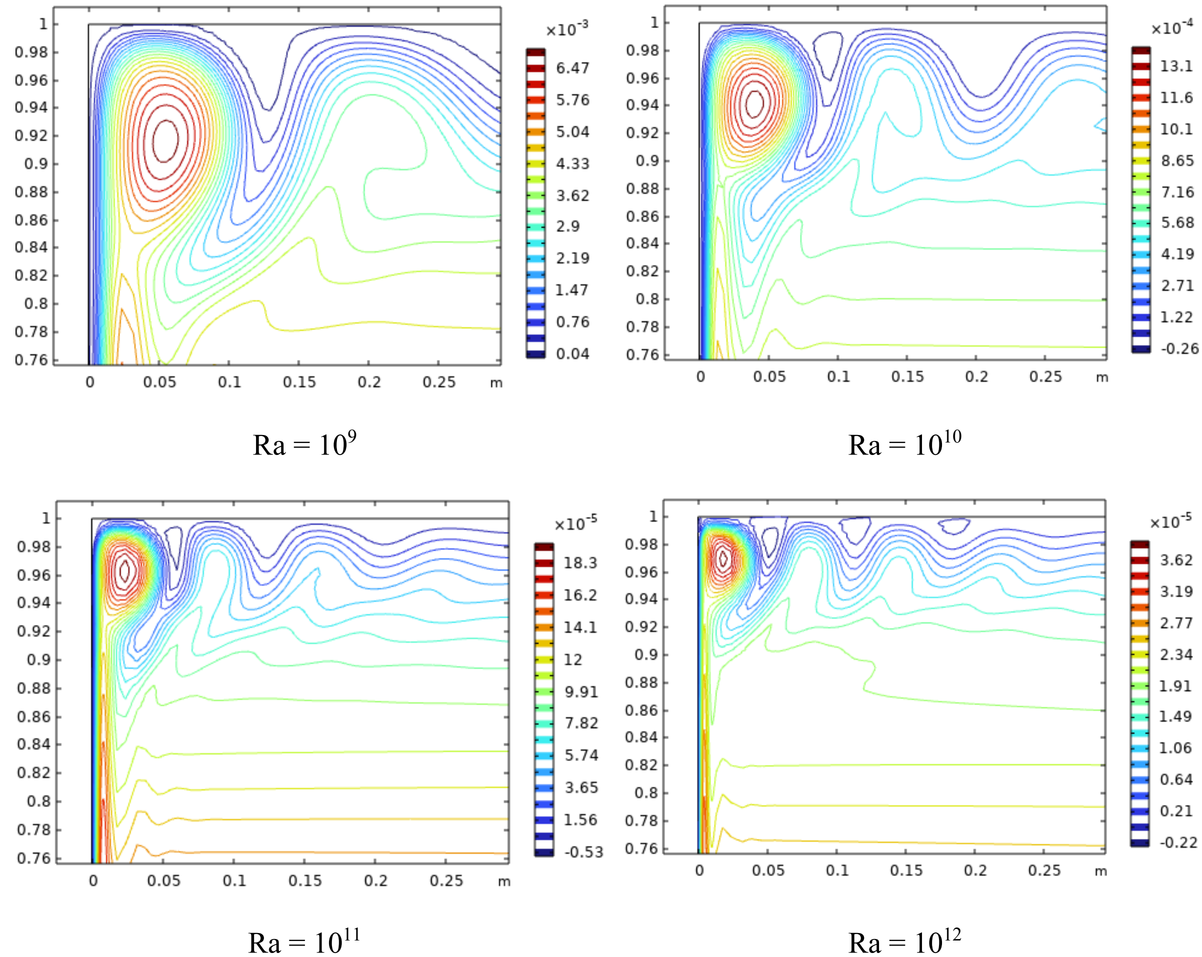

Figure 10. Topology of corner vortices and development of microstructures in the upper-left corner of the cavity for $10^9 \leq \mathrm{Ra} \leq 10^{12}$.

For Ra = 10^9, the formation of a well-defined secondary vortex is observed, with small tertiary recirculation located beneath the main vortex. The layer adjacent to the hot wall is thin but exhibits smooth undulations, with the separation point located very close to the corner (Trias *et al.*, 2007). At Ra = 10^{10}, the secondary vortex becomes more compact and shifts slightly toward the cavity interior; in addition, small-scale vortices develop due to interaction with the upper main circulation (Dixit and Babu, 2006). Transient recirculation vortices also form and dissipate near the corner (Markatos and Pericleous, 1984; Barakos *et al.*, 1994).

The gradient of the stream function increases along the hot wall, which intensifies local velocity gradients and, consequently, the convective contribution to the Nusselt number. At Ra = 10^{11}, the vortical structures exhibit multiscale organization, with a more confined secondary vortex and a lower-intensity tertiary recirculation, arranged as very small-radius microstructures near the wall (Huang *et al.*, 2023; Molina-Herrera and Jiménez-Islas, 2025). Finally, at Ra = 10^{12}, the secondary and tertiary structures become diffuse and millimetric, while heat and momentum transport are dominated by wall-attached currents along the hot vertical surface, defining an almost parallel, stable flow (Ji, 2014; Cintolesi *et al.*, 2015). These results further demonstrate that, at high Rayleigh numbers, refined mesh resolution in the wall-normal direction is essential to accurately capture boundary-layer microstructures, ensure local energy conservation, and obtain numerically robust Nusselt-number values in the highest-Rayleigh-number regime considered in the present two-dimensional study.

4.4 Temperature and stream-function contours

In this section, the dimensionless profiles of temperature θ and velocity components (U_x, U_y) in the X and Y directions are presented and analyzed for the differentially heated cavity over the range Ra = 10^3–10^{12}. Unless otherwise stated, the profiles are extracted along the midlines X = 0.5 and Y = 0.5 and are normalized by the characteristic length. The objective is to characterize the evolution of the thermal

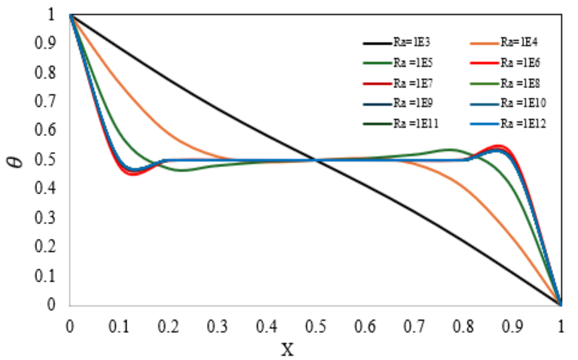

Figure 11. Dimensionless temperature profiles *θ(X)* along the midline $Y = 0.5$ for different Rayleigh numbers.

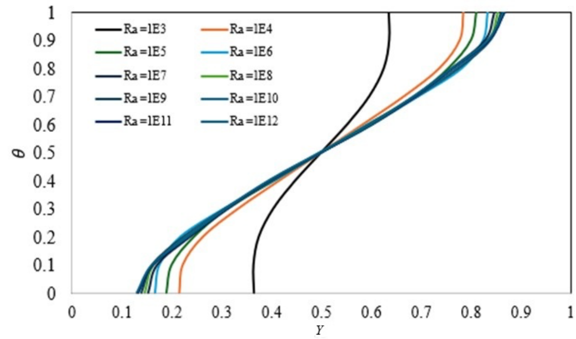

Figure 12. Dimensionless temperature profiles *θ(Y)* along the midline $X = 0.5$, computed for different Rayleigh numbers.

and velocity boundary layers and the stratification of the core region as the Rayleigh number increases. These profiles are fundamental for calculating integral quantities, such as the Nusselt number, and enable assessment of the numerical resolution in near-wall regions, where gradients become increasingly intense (Dixit and Babu, 2006; Goloviznin *et al.*, 2016).

Figure 10 shows the dimensionless temperature profiles *θ(X)* along the horizontal midline $Y = 0.5$, which depicts the physical transition of the system from a nearly pure conduction regime at Ra = 10^3 to a convection-dominated regime as Ra increases. For $10^4 \leq$ Ra $\leq 10^6$, the slope of the temperature profile is concentrated near the hot and cold walls, while the core region exhibits almost isothermal behavior. This indicates the progressive thinning of the thermal boundary layer, a phenomenon consistently reported in classical benchmark studies (De Vahl Davis, 1983).

Figure 11 shows the dimensionless temperature profiles *θ(X)* along the horizontal midline $Y = 0.5$. The profiles clearly depict the orderly physical transition of the differentially heated cavity problem from a nearly pure conduction regime at Ra = 10^3 to a convection-dominated regime as Ra increases. For $10^4 \leq$ Ra $\leq 10^6$, the temperature gradient becomes concentrated near the hot and cold walls, while the core region flattens, indicating a progressively thinner thermal boundary layer, as reported in classical benchmark studies (De Vahl Davis, 1983). In the intermediate-to-high range (Ra = 10^7–10^8), the profiles exhibit local peaks and valleys around $X \approx 0.1$ and $X \approx 0.9$, associated with the interaction between thermal gradients and recirculation cells. This behavior causes the temperature gradient to be confined to a reduced fraction of the characteristic length ($L \approx 0.1$), whereas the cavity core exhibits an almost uniform thermal distribution, with nearly horizontal isotherms that indicate weak thermal stratification of the temperature field (Trias *et al.*, 2007; Dixit and Babu, 2006; Goloviznin *et al.*, 2016).

For high Rayleigh numbers ($10^9 \leq$ Ra $\leq 10^{12}$), the temperature profile exhibits two plateau regions separated by very sharp transitions adjacent to the walls. The dimensionless temperature remains nearly constant in the core region, while the thermal gradient is confined to ultrathin boundary layers near $X \approx 0$ and $X \approx 1$. As Ra increases from 10^{11} to 10^{12}, these transition zones narrow and shift closer to the walls, indicating that heat transfer is primarily concentrated within intense wall-attached convective currents along the differentially heated surfaces. For this reason, the use of refined boundary-layer-type meshes in the wall-normal direction becomes necessary, as they enable accurate resolution of the thermal boundary layers and capture the steep temperature gradients characteristic of a fully developed natural convection regime (Trias *et al.*, 2007; Dixit and Babu, 2006; Goloviznin *et al.*, 2016).

As a complement to the horizontal *θ(X)* profiles, Figure 12 presents the vertical temperature profiles *θ(Y)* along the central line $X = 0.5$ for Ra = 10^3–10^{12}. At Ra = 10^3, the profile exhibits a pronounced curvature with an inflection point located near the center of the domain, indicating that heat transfer is dominated by conduction and that the convective cell exerts a limited influence, slightly modifying the vertical temperature gradient without altering its predominantly conductive character (De Vahl Davis, 1983; Dixit and Babu, 2006; Goloviznin *et al.*, 2016).

As the Rayleigh number increases to Ra = 10^4–10^6, thermal stratification in the core region becomes more pronounced. The profile in the central region approaches a near-linear behavior. In contrast, the thermal transitions shift toward $Y = 0$ and $Y = 1$, evidencing the progressive thinning of the thermal boundary layers at the upper and lower surfaces.

For Ra $\geq 10^7$, the profiles exhibit stable evolution in the core and an almost constant temperature gradient over the interval $0.2 \leq Y \leq 0.8$, with the temperature gradient concentrated in regions adjacent to the differentially heated walls, where convective transport reaches its maximum intensity. These zones of strong thermal gradients correspond to the development of thermal boundary layers, whose progressively thinner thickness with increasing Ra

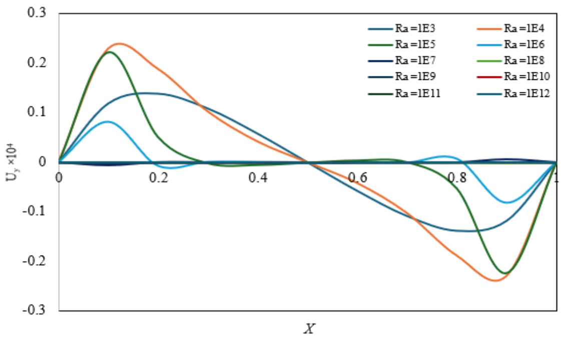

Figure 13. Dimensionless velocity profiles of the U_x component computed at the cavity center for different Rayleigh numbers.

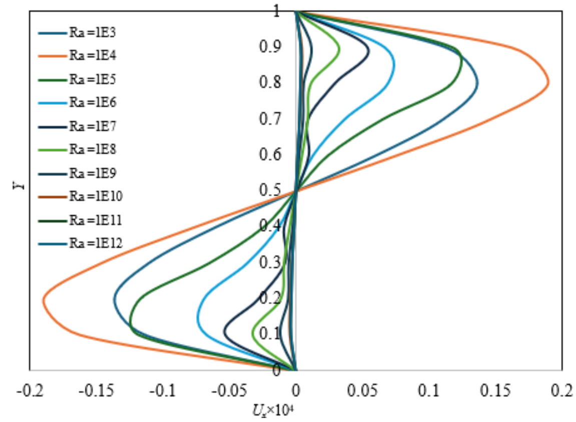

Figure 14. Dimensionless velocity profiles of the U_y component computed at the cavity center for different Rayleigh numbers.

highlights the dominance of the convective regime over the conductive one within the cavity (Dixit and Babu, 2006; Goloviznin *et al.*, 2016). Physically, this behavior indicates that heat transfer is concentrated in regions adjacent to the differentially heated walls. In contrast, the central part of the cavity behaves as a nearly quiescent zone, with small temperature gradients and limited heat transport. This result is consistent with the classical description of the differentially heated cavity problem, in which both heat, and momentum transfer are confined to boundary layers near the walls, while the core maintains an almost isothermal behavior with essentially horizontal isotherms (Igci and Arici, 2016; Dixit and Babu, 2006; Hernández-López *et al.*, 2016).

Figure 13 presents the vertical velocity profiles $U_y(X)$, which exhibit a clear transition from laminar to turbulent flow as the Rayleigh number increases. For Ra $\leq 10^5$, the velocity magnitude increases with the Rayleigh number, reflecting the progressive intensification of natural convection and the presence of recirculation within the domain (Dixit and Babu, 2006; Choi and Kim, 2012). However, for Ra $\geq 10^6$, the profiles change markedly, and the magnitude of U_y decreases in the central region, becoming primarily concentrated in thin layers adjacent to the hot and cold walls. In these regions, the flow is characterized by intense velocity gradients and high viscous dissipation. In contrast, the cavity core exhibits an almost isothermal motion with minimal velocity variation, indicating a quasi-stationary region with weak convective exchange. This behavior is consistent with the observations of De Vahl Davis (1983), who reported that velocity profiles reach their maximum in laminar regimes and tend to stabilize as Ra increases, due to the thinning of both thermal and hydrodynamic boundary layers and the increasing contribution of convective transport in regions adjacent to the hot and cold walls.

In accordance with the above, Dixit and Babu (2006) reported that for Ra ≥ 106, velocities in the core region decrease, and boundary layers dominate transport, concentrating most of the flow near the differentially heated walls. More recently, Goloviznin *et al.* (2016) confirmed that, for Ra $\geq 10^9$, the velocity maxima are located very close to the walls, indicating the progressive thinning of the boundary layers and the fully convective nature of the flow. The results shown in Figure 13, together with the evidence reported in the literature, indicate that as the Rayleigh number increases, the intensity of the vertical flow initially grows but subsequently weakens in the core region, as convection concentrates the thermal and momentum dynamics in regions adjacent to the differentially heated walls, where thin boundary layers develop and are responsible for most of the heat transfer (Hernández-López *et al.*, 2016).

Continuing the analysis of the velocity profiles, Figure 14 presents the horizontal velocity profiles $U_x(Y)$ for different Rayleigh numbers ($10^3 \leq$ Ra $\leq 10^{12}$) along the vertical centerline ($X = 0.5$). At Ra $= 10^3$, the profile is very weak, with low values and no pronounced gradients, indicating an essentially diffusive regime in which natural convection has just begun to develop. In contrast, at Ra $= 10^4$, the most pronounced maxima of Ux appear, reaching higher horizontal velocity values compared with all other Rayleigh numbers. This behavior indicates that within this range, the interaction between conduction and convection enables highly active horizontal transport, associated with large, well-defined recirculation cells (De Vahl Davis, 1983; Dixit and Babu, 2006; Hernández-López *et al.*, 2016; Molina-Herrera and Jiménez-Islas, 2025).

However, as the Rayleigh number increases (Ra $\geq 10^5$), the horizontal velocity profiles decrease in magnitude and become concentrated near the differentially heated walls, where both thermal and velocity boundary layers develop. This behavior indicates that horizontal fluid motion progressively becomes restricted to near-wall regions, while the cavity core loses intensity and becomes more stable. Within this range, natural convection becomes the dominant transport mechanism, concentrating momentum and heat transfer in thin regions near the differentially heated walls (Markatos and Pericleous, 1984; Barakos *et al*., 1994; Hernández-López *et al*., 2016; Molina-Herrera and Jiménez-Islas, 2025).

Figure 14 illustrates this trend for intermediate Rayleigh numbers (Ra = 10^4–10^6), where the profiles exhibit well-defined horizontal maxima associated with large-scale recirculation as Ra increases ($10^7 \leq$ Ra $\leq 10^9$). These maxima decrease, and the profiles become more symmetric and confined, indicating enhanced flow stability in the core region. Finally, for the highest Rayleigh numbers (Ra $\geq 10^{10}$–10^{12}), the amplitude of the profiles is significantly reduced, and velocity variations are almost entirely confined to boundary layers adjacent to the differentially heated walls, where convection is most intense. This behavior reveals a clear transition from a diffusive-convective regime to a fully convective one, in which horizontal velocity patterns evolve from broad distributions with extended recirculation toward narrower profiles concentrated near the differentially heated walls, where velocity and temperature gradients reach their maximum values. In this regime, the flow in the core exhibits a more stable dynamics, and momentum transfer occurs primarily within boundary layers, which become thinner and more intense as the Rayleigh number increases (Goloviznin *et al*., 2016; Hernández-López *et al*., 2016).

Conclusions

A numerical investigation of the classical 2-D differentially heated square cavity was carried out over a wide range of Rayleigh numbers ($10^3 \leq$ Ra $\leq 10^{12}$) using a dimensionless formulation and an orthogonal quadrilateral mesh with boundary-layer refinement in the wall-normal direction. This strategy allowed accurate resolution of the steep thermal and hydrodynamic gradients that develop near the hot and cold walls as the Rayleigh number increases. The predicted Nusselt numbers showed very good agreement with benchmark data reported in the literature, with discrepancies below 1% up to Ra = 10^{11}. At Ra = 10^{12}, a larger difference was observed relative to a high-Rayleigh-number reference; however, the mesh-sensitivity analysis, transient verification, and power-law scaling of the computed dataset all confirmed that the predicted value remains numerically robust within the present two-dimensional framework.

Macroscopic heat-balance verification across the full Rayleigh-number range supported the physical and numerical consistency of the solutions (errors on the order of 10^{-2}), while the transient simulations showed that the steady-state Nusselt values correspond to the long-time asymptotic limit of the same formulation. The computed flow and temperature fields also revealed the progressive strengthening of wall-attached currents and corner recirculation structures as Ra increased, highlighting their direct influence on local thermal gradients and on the global heat-transfer rate. Overall, the results show that the present meshing and solution strategy yield stable, numerically consistent reference results for the classical 2-D cavity benchmark at high Rayleigh numbers. In this sense, the study provides a robust numerical framework for assessing mesh design, convergence behavior, and heat-transfer scaling in the De Vahl Davis problem and offers useful reference data for future two-dimensional benchmark studies and comparisons with more advanced three-dimensional formulations. At the highest Rayleigh numbers considered, these results should be interpreted as benchmark solutions of the adopted two-dimensional formulation, rather than as physically realistic predictions of the fully three-dimensional unsteady cavity flow.

Acknowledgements

The authors acknowledge financial support from SECIHTI through the Postdoctoral Fellowships for the Training and Consolidation of Researchers in Mexico, as well as research funding from TecNM.

Nomenclature

c_p	specific heat, J· kg^{-1}·K^{-1}
g	gravitational acceleration, m·s^{-2}
k	thermal conductivity, J/m·s·K
p	pressure, N·m^2
Pr	Prandtl number, $C_P \cdot \mu/k$
L	length and height of the cavity, m
Nu	average Nusselt number,
ΔT	temperature difference, K
Ra	Rayleigh number, $\rho g \Delta T L^3/\mu\alpha$
T	Temperature, K
T_c, T_h	hot and cold wall temperatures, K
u_{ref}	buoyancy reference velocity, m/s
U_x, U_y, $\overline{U}_x$, $\overline{U}_y$	horizontal and vertical velocity, dimensionless
u_x, u_y, $\overline{u}_x$, $\overline{u}_y$	dimensional horizontal and vertical velocity, m/s
x, y	dimensional coordinates, m
X, Y	dimensionless coordinates

Greek letters

α	thermal diffusivity, m^2/s
β	thermal expansion coefficient, K^{-1}
Δp	drop pressure
ρ	density, kg/m^3

μ dynamic viscosity, kg $m^{-1} \cdot s^{-1}$ or Pa·s
θ dimensionless temperature

Abbreviations

BL	Boundary Layer
FEM	Finite Element Method
NA	Data not available
NC	Convergence not reached
FVM	Finite Volume Method

References

Abbassi, M.A., Safaei, M.R., Djebali, R., Guedri, K., Zeghmati, B., and Alrashed, A.A. (2018). LBM simulation of free convection in a nanofluid filled incinerator containing a hot block. *Int. J. Mech. Sci.* 144, 172–185. https://doi.org/10.1016/j.ijmecsci.2018.05.031

Barakos, G., Mitsoulis, E., and Assimacopoulos, D. (1994). Natural convection flow in a square cavity revisited: laminar and turbulent models with wall functions. *Int. J. Numer. Methods Fluids* 18(7), 695–719. https://doi.org/10.1002/fld.1650180705

Bird, R.B., Stewart, W.E., and Lightfoot, E.N. (2009). *Transport phenomena* (Revised 2nd ed.). John Wiley and Sons, Inc., p. 928.

Cardona, L. M., Cortés-Rodríguez, M., & Castellanos-Galeano, F. J. (2023). *Pineapple powder quality: Effect of the feedstock solution composition, homogenization and spray drying process*. Revista Mexicana de Ingeniería Química, 22(2), Alim2993. https://doi.org/10.24275/rmiq/Alim2993

Castillo, P., and Henríquez, I. (2017). Assessment of time discretizations and LDG methods for diffusion and nonlinear reaction problems in 2D. Rev. Mex. Ing. Quim. 16(2), 541–554. https://www.redalyc.org/pdf/620/62052087019.pdf

Choi, S., and Kim, S. (2012). Turbulence modeling of natural convection in enclosures: a review. *J. Mech. Sci. Technol.* 26(1), 283–297. https://doi.org/10.1007/s12206-011-1037-0

Cintolesi, C., Petronio, A., and Armenio, V. (2015). Large eddy simulation of turbulent buoyant flow in a confined cavity with conjugate heat transfer. *Phys. Fluids* 27(9). https://doi.org/10.1063/1.4930815

Cortés-Avendaño, E. J., Castillo-Zamudio, R. I., Salgado-Cervantes, M. A., and García-Alvarado, M. A. (2023). Heat and mass transfer heterogeneous model applied for mathematical representation of Aloe vera extracts spray drying. Rev. Mex. Ing. Quim. 22(2), Alim237. https://doi.org/10.24275/rmiq/Alim237

De Vahl Davis, G. (1983). Natural convection of air in a square cavity: a benchmark numerical solution. *Int. J. Numer. Methods Fluids* 3(3), 249–264. https://doi.org/10.1002/fld.1650030305

Dixit, H., and Babu, V. (2006). Simulation of high Rayleigh number natural convection in a square cavity using the lattice Boltzmann method. *Int. J. Heat Mass Transf.* 49(3–4), 727–739. https://doi.org/10.1016/j.ijheatmasstransfer.2005.07.046

Dorfman, A., and Renner, Z. (2009). Conjugate problems in convective heat transfer: review. *Math. Probl. Eng.* Volume 2009, Article ID 927350. https://doi.org/10.1155/2009/927350

Duchaine, P. (2010). *Experimental analysis of the dynamics of gaseous and two-phase counterflow flames submitted to upstream modulations* [Doctoral dissertation, Ecole Centrale Paris]. HAL Archives Ouvertes. https://theses.hal.science/tel-00545418v1

El Hattab, M., and Lafdaili, Z. (2022). Turbulent natural convection heat transfer in a square cavity with nanofluids in presence of inclined magnetic field. *Thermal Science* 26(4A), 3201-3213. https://doi.org/10.2298/TSCI210825326E

Ghoben, Z.K., and Hussein, A.K. (2022). The natural convection inside a 3D triangular cross section cavity filled with nanofluid and included cylinder with different arrangements. *Diagnostyka* 23(2), 1–13. https://doi.org/10.29354/diag/149734

Goloviznin, V.M., Korotkin, I.A., and Finogenov, S.A. (2016). Parameter-free numerical method for modeling thermal convection in square cavities in a wide range of Rayleigh numbers. *J. Appl. Mech. Tech. Phys.* 57(7), 1159–1171. https://doi.org/10.1134/s0021894416070063

Henkes, R.A.W.M., and Hoogendoorn, C. (1989). Laminar natural convection boundary-layer flows along a heated vertical plate in a stratified environment. *Int. J. Heat Mass Transf.* 32(1), 147–155. https://doi.org/10.1016/0017-9310(89)90098-7

Hernández-López, I., Xamán, J., Álvarez, G., Chávez, Y., and Arce, J. (2016). Analysis of laminar and turbulent natural, mixed and forced convection in cavities by heatlines. *Arch. Mech.* 68(1), 27–53. https://doi.org/10.24423/aom.1905

Huang, Y., Ge, J., Chen, Y., and Zhang, C. (2023). Natural and forced convection heat transfer characteristics of single-phase immersion cooling systems for data centers. *Int. J. Heat Mass Transf.* 207, 124023. https://doi.org/10.1016/j.ijheatmasstransfer.2023.124023

Igci, A.A., and Arici, M.E. (2016). A comparative study of four low-Reynolds-number k-ε turbulence models for periodically fully developed duct flow and heat transfer. *Numerical Heat Transfer, Part B: Fundamentals* 69(3), 234–248. https://doi.org/10.1080/10407790.2015.1097141

Ji, Y. (2014). CFD modelling of natural convection in air cavities. *CFD Lett.* 6(1), 15–31. Retrieved from https://www.akademiabaru.com/doc/CFDLV6_N1_P15_31.pdf

Jiménez-Islas, H., Calderón-Ramírez, M., Navarrete-Bolaños, J. L., Botello-Álvarez, J. E., Martínez-González, G. M., & López-Isunza, F. (2009). *Numerical study of natural convection in a 2-D square cavity with fluid-porous medium interface and heat generation*. Revista Mexicana de Ingeniería Química, 8(2), 169–185. https://www.scielo.org.mx/pdf/rmiq/v8n2/v8n2a3.pdf

Jiménez-Islas, H., Calderón-Ramírez, M., Molina-Herrera, F., Martínez-González, G., Navarrete-Bolaños, J., and Castrejón-González, E. (2014). Low-RAM algorithm for solving 3-D natural convection problems using orthogonal collocation. *Rev. Mex. Ing. Quim.* 13(1), 259–277. https://www.redalyc.org/pdf/620/62031166020.pdf

Jones, W., and Launder, B. (1972). The prediction of laminarization with a two-equation model of turbulence. *Int. J. Heat Mass Transf.* 15(2), 301–314. https://doi.org/10.1016/0017-9310(72)90076-2

Markatos, N., and Pericleous, K. (1984). Laminar and turbulent natural convection in an enclosed cavity. *Int. J. Heat Mass Transf.* 27(5), 755–772. https://doi.org/10.1016/0017-9310(84)90145-5

Molina-Herrera, F.I., Quemada-Villagómez, L.I., Navarrete-Bolaños, J.L., and Jiménez-Islas, H. (2024). Comparative analysis of nondimensionalization approaches for solving the 2-D differentially heated cavity problem. *Int. J. Numer. Methods Fluids* 96(7), 1276–1303. https://doi.org/10.1002/fld.5285

Molina-Herrera, F.I., and Jiménez-Islas, H. (2025). Direct numerical simulation of the differentially heated cavity and comparison with the κ-ε model for high Rayleigh numbers. *Modelling,* 6(3), 66. https://doi.org/10.3390/modelling6030066

Orszag, S.A. (1970). Analytical theories of turbulence. *J. Fluid Mech.* 41(2), 363-386. https://doi.org/10.1017/S0022112070000642

Trias, F.X., Soria, M., Oliva, A., and Pérez-Segarra, C.D. (2007). Direct numerical simulations of two- and three-dimensional turbulent natural convection flows in a differentially heated cavity of aspect ratio 4. *J. Fluid Mech.* 586, 259–293. https://doi.org/10.1017/S0022112007006908

Trias, F.X., Gorobets, A., Soria, M., and Oliva, A. (2010). Direct numerical simulation of a differentially heated cavity of aspect ratio 4 with Rayleigh numbers up to 10^{11} – Part I: Numerical methods and time-averaged flow. *Int. J. Heat Mass Transf.* 53(4), 665-673. https://doi.org/10.1016/j.ijheatmasstransfer.2009.10.026

Villa Ortiz, A., and Koloszar, L. (2023). RANS thermal modelling of a natural convection boundary layer at low Prandtl number. *Comput. Fluids* 254, 105809. https://doi.org/10.1016/j.compfluid.2023.105809

Welti-Chanes, J., Gómez-Palomares, O., Vergara-Balderas, F., & Maris-Alzamora, S. (2005). *Engineering and transport phenomena applications to convective heat transfer study for canned foods*. *Rev. Mex. Ing. Quim.* 4, 89–106. https://rmiq.org/iqfvp/Pdfs/Vol.%204,%20No.%201/7.pdf

Wilcox, D.C. (1993). *Turbulence modeling for CFD.* Retrieved from http://ci.nii.ac.jp/ncid/BA21991687

Weppe, A., Moreau, F., and Saury, D. (2022). Experimental investigation of a turbulent natural convection flow in a cubic cavity with an inner obstacle partially heated. *Int. J. Heat Mass Transf.* 194, 123052. https://doi.org/

10.1016/j.ijheatmasstransfer.2022.123052

Xin, S., and Le Quéré, P. (1994). Numerical simulations of 2D turbulent natural convection in differentially heated cavities of aspect ratios 1 and 4. *Fluid Mechanics and Its Applications*, 423–434. https://doi.org/10.1007/978-94-011-1000-6_36

Zamora-Cisneros, D. U., & Ruiz Martínez, R. S. (2023). *Simulation investigation of oxydehydrogenation of ethane in an industrial-scale turbulent fluidized bed over MoVTeNbO catalyst*. *Revista Mexicana de Ingeniería Química*, 22(2), Cat2312. https://doi.org/10.24275/rmiq/Cat2312